Harnessing coherent-wave control for sensing applications

Pablo Jara,[1,*] Arthur Goetschy,[2] Hui Cao,[3] and Alexey Yamilov[1,†]

[1] *Department of Physics, Missouri University of Science and Technology, Rolla, Missouri 65409, USA*
[2] *ESPCI ParisTech, PSL Research University, CNRS, Institut Langevin, F-75005 Paris, France*
[3] *Department of Applied Physics, Yale University, New Haven, Connecticut 06520, USA*

(Received 1 July 2025; revised 25 September 2025; accepted 16 October 2025; published 10 November 2025)

Imaging techniques such as functional near-infrared spectroscopy and diffuse optical tomography (DOT) achieve deep, noninvasive sensing in turbid media; however, they are constrained by the photon budget, as most of the injected light is lost to scattering before reaching the detector. Wavefront shaping (WFS) can enhance signal strength via interference at specific locations within scattering media, enhancing light-matter interactions and potentially extending the penetration depth of these techniques. Interpretation of the resulting measurements relies on knowing the optical sensitivity—the relationship between changes in the detected signals and perturbations at a specific location inside the medium; however, conventional diffusion-based sensitivity models rely on assumptions that become invalid under coherent illumination. In this work, we develop a microscopic theory for optical sensitivity that captures the inherent interference effects that diffusion theory necessarily neglects. We show analytically that, under disorder averaging with random illumination, the microscopic and diffusive descriptions coincide. Beyond this limit, our framework identifies WFS strategies that enhance sensitivity. We demonstrate that the input state obtained through phase conjugation at a given point inside the system leads to the largest enhancement of optical sensitivity but requires an input wavefront that depends on the target position. In sharp contrast, the maximum remission eigenchannel, corresponding to the largest eigenvalue of the monochromatic remission matrix, leads to a global enhancement of the sensitivity map with a fixed input wavefront. This global enhancement equals the remission enhancement and preserves the spatial distribution of the sensitivity, making it compatible with existing DOT reconstruction algorithms. Our results, validated through extensive numerical simulations, establish the theoretical foundation for integrating wavefront control with diffuse optical imaging, enabling deeper tissue penetration through improved signal strength in biomedical applications.

DOI: 10.1103/wwbs-pftg

I. INTRODUCTION

In optics, acoustics, seismology, microwave physics, and other fields, scattered waves serve as versatile noninvasive probes for a stand-off characterization of complex scattering systems [1–4]. While both electromagnetic waves and sound waves are extensively used in medical imaging [5], optical methods operating in the near-infrared regime offer unique advantages for probing biological tissue, combining molecular specificity with deep penetration [6]. Ballistic or nearly ballistic photon imaging methods such as optical coherence tomography offer high spatial resolution but they are limited to essentially superficial tissue layers [7]. Diffuse optical tomography (DOT) and functional near-infrared spectroscopy extract information from multiply scattered light, enabling interrogation of much larger depths [8–12] aided by reduced attenuation in the near-infrared spectral-transparency window in biological materials [13]. These techniques operate in *remission geometry*, which involves injecting near-infrared light into tissue at a source position, while collecting the multiply scattered photons that emerge at a detector placed at a different location on the tissue surface. The detected light signals from multiple source-detector pairs are then used to reconstruct the spatial distribution of tissue optical properties through inverse-problem techniques [14,15]. Therefore, the success of DOT-based approaches hinges on two key principles [10]: (1) the ability to predict how local changes in tissue properties modulate the detected signal (sensitivity) [16], and (2) the ability to reconstruct the photon propagation paths connecting sources to detectors (inverse problem). The omnidirectional nature of diffuse light propagation leads to a decrease of signal strength with both depth and source-detector separation [9], whereas the maximum input intensity is limited by

*Contact author: pxjdbk@mst.edu
†Contact author: yamilov@mst.edu

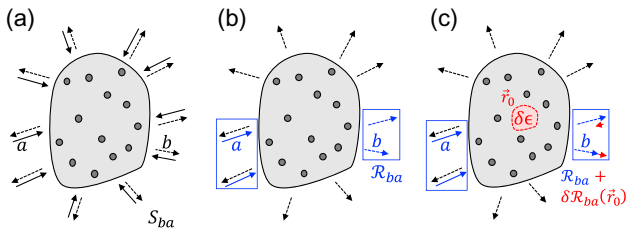

FIG. 1. Schematic of scattering approach. (a) Scattering matrix element S_{ba} relates the field amplitudes of the incident mode a (solid line arrows) and the outgoing mode b (dashed arrows). (b) Experimentally, one has access to a finite number of spatial channels (blue arrows), described by the matrix $\mathcal{R}_{ba}$, which is a subset of S. (c) The addition of a small perturbation to the dielectric properties inside the system results in a change $\delta\mathcal{R}_{ba}(\mathbf{r}_0)$, which depends on its location $\mathbf{r}_0$.

tissue damage thresholds [17]. A fixed photon budget ultimately constrains the maximum depth accessible by DOT-based approaches [18,19].

Wavefront shaping (WFS) techniques [20–24] have emerged as a promising avenue for enhancing the signal strength at depth [25,26]. This is expected to enhance light-matter interaction and hence increase modulation of the remitted signal; however, the intensity patterns created inside the scattering medium can no longer be adequately described by diffusion theory [27–31], nor can the relationship between signal modulation and the underlying perturbation be justified [32] using traditional diffusion-based approaches [10]. These observations put into question the applicability of diffusion-based interpretation of the sensitivity map when used in conjunction with WFS input.

To formally describe wave transport through complex media, it is useful to adopt a scattering framework. Element S_{ba} of a scattering matrix describes the amplitude of the wave scattered by the system into spatial channel b (e.g., the wave-vector direction), upon a coherent excitation via channel a [33,34] [see Fig. 1(a)]. Commonly, the experimental setup for interrogation of the scattering system involves detection of a subset of all incoming and outgoing waves [22], $\mathcal{R}_{ba}$ [Fig. 1(b)]. Sensitivity analysis [10,14,15,35] is a powerful tool that is used to characterize the variations in local properties of complex medium, e.g., in the real or imaginary part of the dielectric function $\delta\epsilon$ at a spatial position $\mathbf{r}_0$ through detection of changes $\delta\mathcal{R}_{ba}(\mathbf{r}_0)$ in scattered amplitudes [Fig. 1(c)].

An important insight into the problem has been obtained recently in Ref. [32], where wavefront control technique was applied to the continuous-wave (CW) matrix $\mathcal{R}$ defined specifically in the remission geometry—a configuration involving a semi-infinite medium where both source and detector lie on the same side of the sample. In the equation $\mathbf{E}_{\text{out}} = \mathcal{R}\,\mathbf{E}_{\text{in}}$, the matrix operator relates the incident field $\mathbf{E}_{\text{in}}$ and remitted field $\mathbf{E}_{\text{out}}$, which can be decomposed into N_1 and N_2 spatial channels, e.g., flux-carrying modes of the optical fibers in DOT. As could be expected, the numerical and experimental results indeed demonstrated a significant (one order of magnitude) enhancement of the remitted signal by exciting the highest remission eigenchannel, whose input wavefront is given by the eigenvector of $\mathcal{R}^\dagger\mathcal{R}$, corresponding to its largest eigenvalue. Importantly, a new *microscopic* formulation based on the scalar wave equation was proposed to obtain the sensitivity map [32]. Remarkably, it was found that the *spatial distribution* of the sensitivity map for the maximum remission eigenchannel (MRE) remained the same as that for random input, while the *magnitude* of the sensitivity enhancement was nearly equal to the magnitude of the remission enhancement. These findings suggest the possibility of extending the diffusion-based DOT treatments to include WFS excitation. Indeed, if the sensitivity magnitude could be computed theoretically, while the inverse-problem solution could use the same sensitivity map found in the diffusion model, coherent enhancement of the remitted signal would immediately translate into deeper noninvasive sensing and imaging in biological media.

While the results in our previous work [32] provided an important clue into how optical sensitivity is affected by coherent control, a comprehensive study is required to formulate a new approach and validate its applicability. First, the microscopic theory must be rigorously tested against the widely used diffusion-based approach; for example, for random input excitation, the field-based approach should reduce to diffusion theory. Second, the dependence of the sensitivity on key system parameters such as the transport mean free path and source-detector geometry needs systematic verification. It also remains unclear what the optimal strategy is for enhancing optical sensitivity within the context of wavefront shaping. Furthermore, since coherent WFS can manipulate the amplitude, phase, and polarization of incident waves, extension of the scalar wave theory to incorporate the full vectorial nature of the electromagnetic waves is essential for a complete theoretical description of optical sensitivity.

In this work, we present a comprehensive study of CW optical sensitivity in complex media, focusing on the role of wavefront shaping in enhancing detection capabilities. In Sec. II, we derive analytical expressions for sensitivity using a microscopic approach that remains valid even when coherent wavefront shaping is employed. We establish a connection between optical sensitivity and phase conjugation [36,37], demonstrating how tailored input wavefronts can maximize the system's response to perturbations. In Sec. III, we perform numerical simulations to validate our theoretical predictions, comparing the sensitivity enhancements achieved through different excitation schemes. We further investigate how sensitivity enhancement scales with system parameters such as the

transport mean free path and the source-detector geometry. In Sec. IV, we extend our analysis to vector electromagnetic waves and demonstrate that the key results remain consistent with those derived for scalar waves. Our findings provide a theoretical foundation for understanding sensitivity in coherent wave transport, offer insights into different wavefront shaping strategies, and pave the way for next-generation diffuse optical imaging techniques.

II. OPTICAL SENSITIVITY: ANALYTICAL RESULTS FOR SCALAR WAVES

In this section, we consider scalar waves and derive analytical expressions for the CW optical sensitivity using a unified approach requiring minimal assumptions. In Sec. II A, we present a derivation of sensitivity that applies to arbitrary system geometries and does not rely on the diffusion approximation. In Sec. II B, we then establish the connection between optical sensitivity and phase conjugation, describing the construction of such a wavefront and demonstrating the enhancement of sensitivity. In Sec. II C, we develop the disorder-averaged intensity sensitivity model, which requires the additional assumptions that the input wavefront is uncorrelated with the disordered system and that wave transport is diffusive. We prove analytically in Sec. II D that under random excitation, these two models lead to identical results in diffusive media. We conclude in Sec. II E by introducing normalized sensitivity and discuss its advantages in sensitivity analyses.

A. Microscopic approach to optical sensitivity

We consider a CW monochromatic scalar field $E_0(\mathbf{r})$ in a medium with dielectric function $\epsilon(\mathbf{r})$, representing one realization of disorder. The unperturbed field satisfies the wave equation

$$\left[\nabla^2 + k^2\epsilon(\mathbf{r})\right] E_0(\mathbf{r}) = 0, \tag{1}$$

where $k = 2\pi/\lambda_0$ is the wave number in vacuum and $\epsilon(\mathbf{r})$ is a spatially varying dielectric function of the medium. A small perturbation $\delta\epsilon(\mathbf{r})$ near $\mathbf{r}_0$ modifies the wave equation, resulting in a new solution $E(\mathbf{r})$. The change in the field $\delta E(\mathbf{r}) \equiv E(\mathbf{r}) - E_0(\mathbf{r})$ can be written using the Lippmann-Schwinger equation:

$$\delta E(\mathbf{r}) = \int d\mathbf{r}'\, G_0(\mathbf{r},\mathbf{r}')\, \mathcal{V}(\mathbf{r}')\, E(\mathbf{r}'). \tag{2}$$

Here, we adopted the language of the scattering theory, where $G_0 = (k^2 - H_0)^{-1}$ is the (retarded) Green's function of the original wave equation, with $H_0 = -\nabla^2 - k^2[\epsilon(\mathbf{r}) - 1]$ and $\mathcal{V}(\mathbf{r}) = -k^2\delta\epsilon(\mathbf{r})$. In the Born approximation, and assuming a pointlike perturbation at $\mathbf{r}_0$, we set $\delta\epsilon(\mathbf{r}) = \delta\epsilon\, \delta V \delta(\mathbf{r} - \mathbf{r}_0)$, yielding

$$\delta E(\mathbf{r}) \simeq \tilde{\mathcal{V}}\, G_0(\mathbf{r},\mathbf{r}_0) E_0(\mathbf{r}_0), \tag{3}$$

where $\tilde{\mathcal{V}} = -k^2\delta\epsilon\, \delta V$ is the strength of the perturbation and δV represents an effective volume associated with the perturbation.

The above expression, given in the position representation $E(\mathbf{r}) = \langle \mathbf{r}|E\rangle$, also holds in any representation $E(\psi) = \langle\psi|E\rangle$. This allows us to cast the problem in the language of optical tomography. To this end, we evaluate the variation of the flux F received by a detector [Fig. 1(c)] in the basis of flux-normalized output modes $\{|\psi_b\rangle\}$,

$$\delta F = \sum_{b=1}^{N_2} |\langle\psi_b|E\rangle|^2 - |\langle\psi_b|E_0\rangle|^2 \simeq \sum_{b=1}^{N_2} 2\mathrm{Re}\left[\delta E_b\, u_b^*\right], \tag{4}$$

where $u_b = \langle\psi_b|E_0\rangle$ in the output field measured in the channel b and

$$\delta E_b = \frac{\tilde{\mathcal{V}}}{2i}\, \phi_b(\mathbf{r}_0)\, E_0(\mathbf{r}_0). \tag{5}$$

Here, $\phi_b(\mathbf{r}_0) = 2i\langle\psi_b|G_0|\mathbf{r}_0\rangle$ represents the field in channel b when excited by a pointlike source at $\mathbf{r}_0$ [38]. By reciprocity, it is also the field at $\mathbf{r}_0$ when channel b is excited from the output port. As flux-normalized states $\psi_b(\mathbf{r})$ are related to intensity-normalized states $\chi_b(\mathbf{r})$ according to $\psi_b(\mathbf{r}) = \chi_b(\mathbf{r})/\sqrt{k_b^z}$, where k_b^z is the longitudinal component of the momentum of $\chi_b(\mathbf{r})$, we can also write $\phi_b(\mathbf{r}_0) = 2i\sqrt{k_b^z}\langle\mathbf{r}_0|G_0|\chi_b\rangle = 2ik_b^z\langle\mathbf{r}_0|G_0|\psi_b\rangle$. Substituting Eq. (5) into Eq. (4) gives

$$\delta F \simeq \mathrm{Re}\left[-i\,\tilde{\mathcal{V}}\,\phi(\mathbf{r}_0)\, E_0(\mathbf{r}_0)\right], \tag{6}$$

where we introduced the notation

$$\phi(\mathbf{r}_0) = \sum_{b=1}^{N_2} u_b^*\, \phi_b(\mathbf{r}_0), \tag{7}$$

and summation over b runs over N_2 output channels.

To complete the derivation, we use Eq. (6) and formally define the optical sensitivity to a *local absorber* with $\delta\epsilon = i\epsilon''$ as

$$\mathcal{S}(\mathbf{r}_0) \equiv \frac{dF(\mathbf{r}_0)}{d\epsilon''} = -k^2\, \delta V \mathrm{Re}\left[\phi(\mathbf{r}_0) E_0(\mathbf{r}_0)\right]. \tag{8}$$

This expression [32] serves as the foundation for the analysis that follows.

It is illuminating to express the input state used to excite $E_0(\mathbf{r})$ in terms of N_1 flux-normalized input channels $\{|\psi_a\rangle\}$ as $\left|\psi^{\mathrm{in}}\right\rangle = \sum_{a=1}^{N_1} v_a\, |\psi_a\rangle$. Here, v_a are amplitudes of each

mode satisfying the constraint $\sum_{a=1}^{N_1}|v_a|^2 = N_1$. Therefore, $E_0(\mathbf{r}_0) = \sum_{a=1}^{N_1} v_a\phi_a(\mathbf{r}_0)$, similar to the output states introduced in Eq. (7). We find

$$\mathcal{S}(\mathbf{r}_0) = -k^2\delta V \sum_{baa'} \mathrm{Re}\left[\phi_b(\mathbf{r}_0)\mathcal{R}^*_{ba'}\phi_a(\mathbf{r}_0)v^*_{a'}v_a\right], \quad (9)$$

where we took advantage of the relationship $u_b = \sum_{a=1}^{N_1}\mathcal{R}_{ba}v_a$. We note that Eqs. (8) and (9) are, in fact, equivalent.

We end this section with several comments. First, Eqs. (8) and (9) are obtained in the Born approximation (weak perturbation), which means that they become exact in the limit $k^{\mathcal{D}}\,\delta V\epsilon'' \ll 1$, where $\mathcal{D} = 2, 3$ is the dimensionality of the system. Second, the sensitivity in Eqs. (8) and (9) is expressed in terms of complex-valued fields and coefficients $\{\phi(\mathbf{r}_0), E_0(\mathbf{r}_0)\}$ or $\{\phi_a(\mathbf{r}_0), \phi_b(\mathbf{r}_0), v_a, \mathcal{R}_{ba}\}$, respectively, all computed (or, in the case of v_a, specified) for the same realization of disorder. To compute the statistically averaged sensitivity from Eqs. (8) and (9), one must ensemble-average the full product of fields in the sensitivity expression rather than averaging the fields themselves. This distinction preserves interference effects that contribute to coherent transport, even after disorder averaging. Lastly, we note that $\mathcal{S}(\mathbf{r}_0)$ has an implicit dependence on the location of the perturbation center that makes it a *sensitivity map*: *external* measurement of the flux contains information about the *internal* location $\mathbf{r}_0$ of the perturbation. It is this key feature that enables noninvasive approaches to tomographic reconstruction of the optical properties of the medium.

B. Phase conjugation and optical sensitivity

Equation (9) shows that the ability to enhance optical sensitivity at a target position $\mathbf{r}_0$ within a scattering medium hinges on a judicial choice of the input wavefront defined by the coefficients v_a. Among various wavefront-shaping strategies, phase conjugation (PC) appears as a particularly intuitive and effective approach [23,36,39–41]. Indeed, in a complex medium, a point source at $\mathbf{r}_0$ generates a wavefront that propagates outward, undergoing multiple scattering events. The phase-conjugated input, constructed by reversing the outgoing wavefront detected at the position of our extended source, excites a field that naturally retraces these scattering paths in a time-reversed fashion. This is a consequence of the time-reversal symmetry [37,42] in CW propagation. Refocusing energy back at $\mathbf{r}_0$ is not perfect because time reversal of partial outgoing waves is incomplete. It is expected that this constructive interference should maximize the local field amplitude for a given amount of finite control, thereby amplifying the response to small perturbations in the optical properties at $\mathbf{r}_0$—a concept that has been formalized using the generalized Wigner-Smith operator and related optimal input states [43–46]. The modal coefficients for the PC wavefront are given, in our notation, by

$$v_a^{\mathrm{PC}} = \left[\frac{N_1}{I_{\mathrm{in}}(\mathbf{r}_0)}\right]^{1/2}\phi_a^*(\mathbf{r}_0), \quad (10)$$

where $I_{\mathrm{in}}(\mathbf{r}_0) = \sum_{a=1}^{N_1}|\phi_a(\mathbf{r}_0)|^2$, and the $N_1^{1/2}$ factor ensures that the total input flux remains equal to N_1, following the convention adopted earlier. By substituting Eq. (10) into Eq. (9), the sensitivity with PC input becomes

$$\mathcal{S}^{\mathrm{PC}}(\mathbf{r}_0) = -N_1k^2\delta V\sum_{ba}\mathrm{Re}\left[\phi_b(\mathbf{r}_0)\mathcal{R}^*_{ba}\phi_a(\mathbf{r}_0)\right]. \quad (11)$$

To put this result into perspective, we obtain an expression for sensitivity under two alternative excitation schemes. First, we consider a random combination of input channels, such that $\overline{v^*_{a'}v_a} = \delta_{a'a}$. Here, the averaging is performed only over different combinations of random inputs in a particular realization of the system—i.e., no disorder ensemble average is assumed. In this case Eq. (9) yields

$$\begin{aligned}\mathcal{S}^{\mathrm{RI}}(\mathbf{r}_0) &= -k^2\delta V\sum_{ba}\mathrm{Re}\left[\phi_b(\mathbf{r}_0)\mathcal{R}^*_{ba}\phi_a(\mathbf{r}_0)\right]\\ &= \mathcal{S}^{\mathrm{PC}}(\mathbf{r}_0)/N_1. \end{aligned}\quad (12)$$

Here, the superscript RI indicates a random input. Remarkably, we observe that excitation with PC leads to enhancement of sensitivity by a factor of N_1 compared to random input. While such an enhancement might be expected, it is, in fact, a highly nontrivial result. Phase conjugation is well known to enhance the *intensity* at the target location by such a factor due to constructive interference. In the case of optical sensitivity, however, the quantity of interest involves a product of two distinct fields [see Eqs. (8) and (9)]: one propagating from the injection site and the other from the detection port. An enhancement of the field originating from the source is expected, given that phase conjugation directly optimizes energy delivery to $\mathbf{r}_0$. Surprisingly, the second field, originating from the detection site, is also enhanced by the same factor. This outcome is not obvious, as the back-propagating field is not directly controlled by the phase-conjugated input. Instead, its enhancement arises due to the intrinsic reciprocity of wave propagation in complex media, which ensures that the time-reversed wavefront optimally reconstructs the field at the target location, thereby reinforcing the response to perturbations and leading to the obtained sensitivity enhancement.

In our previous work [32], we demonstrated enhancement of sensitivity when the system was excited by singular vectors of the remission matrix $\mathcal{R}$. In this scheme, we

use the singular value decomposition of $\mathcal{R}$,

$$\mathcal{R}_{ba} = \sum_{\alpha=1}^{\min(N_1,N_2)} U_{b\alpha}\rho_\alpha^{1/2}V_{\alpha a}^*, \tag{13}$$

and select a specific $\alpha = 1$—the MRE. We chose $v_a = N_1^{1/2}\,V_{a1}$—the first column of the $V_{a\alpha}$ matrix, which corresponds to the maximum remission eigenvalue ρ_1. Here, by adding the factor $N_1^{1/2}$, we ensure that the total flux used to excite the system is equal to N_1, i.e., $\sum_{a=1}^{N_1}|v_a|^2 = N_1$, as in the previous two schemes [Eqs. (11) and (12)]. Substituting this input vector into Eq. (9), and taking advantage of the unitarity of the U and V matrices in Eq. (13), we obtain

$$\mathcal{S}^{\mathrm{MRE}}(\mathbf{r}_0) = -N_1k^2\delta V\sum_{ab}\mathrm{Re}\left[\phi_b(\mathbf{r}_0)\left(V_{a1}\rho_1^{1/2}U_{1b}^*\right)\phi_a(\mathbf{r}_0)\right]. \tag{14}$$

Comparing the above to Eqs. (11) and (13), we observe that excitation of the remission eigenchannel amounts to the replacement $\mathcal{R}_{ba} = \sum_\alpha U_{b\alpha}\rho_\alpha^{1/2}V_{\alpha a}^* \to \left(V_{a1}\rho_1^{1/2}U_{1b}^*\right)$ in the PC expression for sensitivity. In other words, in selecting MRE, we are singling out the largest singular value contribution to the remission matrix and omitting the rest.

Several remarks are in order. First, we would like to stress that similar to Eq. (9), all of Eqs. (11), (12), and (14) hold in the single realization of the scattering system; i.e., no ensemble averaging is assumed.

Second, our result above suggests that

$$|\bar{\mathcal{S}}^{\mathrm{RI}}(\mathbf{r}_0)| < |\bar{\mathcal{S}}^{\mathrm{MRE}}(\mathbf{r}_0)| < |\bar{\mathcal{S}}^{\mathrm{PC}}(\mathbf{r}_0)|, \tag{15}$$

with the overline denoting statistical averaging. Hence, the phase-conjugation approach indeed leads to the highest sensitivity for a given point $\mathbf{r}_0$. While the strict ordering $|\mathcal{S}^{\mathrm{RI}}(\mathbf{r}_0)| < |\mathcal{S}^{\mathrm{MRE}}(\mathbf{r}_0)| < |\mathcal{S}^{\mathrm{PC}}(\mathbf{r}_0)|$ probably holds in a typical sense, it is important to clarify that the relation between MRE and RI, and between MRE and PC, might not be guaranteed for a single realization of disorder. Unlike PC excitation, which deterministically enhances sensitivity by a factor of N_1 above the RI result, the MRE scheme involves interference effects determined by the eigenvectors of the remission matrix. As a result, $\mathcal{S}^{\mathrm{MRE}}(\mathbf{r}_0)$ is not guaranteed to be negatively defined and can exhibit significant fluctuations due to disorder-specific interference effects; however, on average, $|\bar{\mathcal{S}}^{\mathrm{MRE}}(\mathbf{r}_0)|$ exceeds $|\bar{\mathcal{S}}^{\mathrm{RI}}(\mathbf{r}_0)|$ by a factor approximately equal to the remission enhancement, as shown in Ref. [32] and later in this work.

Third, the *enhancement of sensitivity* $\eta_{\mathcal{S}}^{\mathrm{PC}}(\mathbf{r}_0) \equiv \mathcal{S}^{\mathrm{PC}}(\mathbf{r}_0)/\mathcal{S}^{\mathrm{RI}}(\mathbf{r}_0)$ in the phase-conjugation scheme (N_1) exceeds that for the largest remission eigenchannel $\eta_{\mathcal{S}}^{\mathrm{MRE}}(\mathbf{r}_0) \equiv \mathcal{S}^{\mathrm{MRE}}(\mathbf{r}_0)/\mathcal{S}^{\mathrm{RI}}(\mathbf{r}_0)$ (see for example Ref. [32]). As can be seen from Eq. (10), to achieve the largest sensitivity, the phase-conjugation scheme requires an input vector uniquely tailored to the specific observation point $\mathbf{r}_0$. In contrast, remission eigenchannels are computed based on $\mathcal{R}_{ba}$, which is a *global* quantity, independent of $\mathbf{r}_0$. As such, the largest remission eigenchannels lead to a global enhancement of sensitivity with a position-independent input vector [32] (see Sec. II D). The ability to enhance sensitivity globally in a complex scattering system with a fixed input wavefront is highly nontrivial. This effect is captured by the filtered random matrix theory (see Appendix G) in diffusive systems, which we turn to next.

C. Diffusion approximation for optical sensitivity

Having established a general formulation of optical sensitivity in arbitrary geometry, we now examine its implications in the diffusive regime, where light transport follows a statistical description. In this section, we derive the corresponding sensitivity expressions within diffusion theory, providing a benchmark for comparison with the more general microscopic approach (see for example Ref. [10]). Seminal contributions to sensitivity analysis in the diffusive regime have been made by J. Schotland and collaborators, particularly in the context of inverse problems and optical tomography [14,15,35,47,48]. Unlike in Sec. II A, the starting point of this consideration is the diffusion equation and not the wave equation. We begin by discussing the assumptions enabling such an approach. First, the diffusion equation describes disorder-averaged quantities such as intensity $\bar{I}(\mathbf{r})$ denoted with an overline. Second, such a description is applicable at scales much larger than the transport mean free path ℓ. Therefore, it is assumed here that relevant length scales, such as the system size and the separation distance between the source and the detector, are much larger than ℓ [49].

Let us first consider the case without any perturbation. The input state is expressed in terms of the N_1 flux-normalized input channels $\{|\psi_a\rangle\}$ and is assumed to be uncorrelated with the disordered system. The mean flux in the output port then reads

$$\bar{F} = \sum_{a,b}\overline{|\mathcal{R}_{ba}|^2}\,|v_a|^2. \tag{16}$$

The elements of the remission matrix $\mathcal{R}_{ba}$ describing scattering from channel a to channel b [Fig. 1(c)] can be expressed using the Fisher-Lee relation [38]

$$\mathcal{R}_{ba} = 2i\sqrt{k_a^z k_b^z}\langle\chi_b|G_0|\chi_a\rangle. \tag{17}$$

The flux in Eq. (16) contains the disorder-averaged product of two *field* Green's functions G_0. It can be evaluated

within the diffusion framework, which amounts to keeping only the so-called ladder diagrams in the Bethe-Salpeter equation [33,49,50]. We obtain

$$\overline{|\mathcal{R}_{ba}|^2} = 4k_a^z k_b^z \int d\mathbf{r}_1\, d\mathbf{r}_2\, \left|\langle\chi_b|\overline{G}_0|\mathbf{r}_2\rangle\right|^2 \Gamma(\mathbf{r}_2,\mathbf{r}_1)\, \left|\langle\mathbf{r}_1|\overline{G}_0|\chi_a\rangle\right|^2, \tag{18}$$

where the kernel $\Gamma(\mathbf{r}_2,\mathbf{r}_1)$ obeys the stationary diffusion equation

$$-D\nabla^2\Gamma(\mathbf{r}_2,\mathbf{r}_1) = \frac{\gamma}{\tau}\delta(\mathbf{r}_2-\mathbf{r}_1). \tag{19}$$

Here, $D = \ell v_E/\mathcal{D}$ is the diffusion constant, in which v_E is the energy velocity, $\tau = \ell/v_E$ is the scattering time, and γ is the scattering strength. The latter can be expressed in terms of ℓ and the mean density of states $\mathrm{DOS}(\omega)$ as

$$\gamma = \frac{2k^2}{\pi c\ell\,\mathrm{DOS}(\omega)}. \tag{20}$$

The presence of the perturbation at $\mathbf{r}_0$ results in a modification of the *mean*, disorder-averaged, flux at the output as

$$\delta\overline{|\mathcal{R}_{ba}|^2} = 4k_a^z k_b^z \int d\mathbf{r}_1\, d\mathbf{r}_2\, \left|\langle\chi_b|\overline{G}_0|\mathbf{r}_2\rangle\right|^2 \delta\Gamma(\mathbf{r}_2,\mathbf{r}_1)\, \left|\langle\mathbf{r}_1|\overline{G}_0|\chi_a\rangle\right|^2. \tag{21}$$

The change in the diffusive kernel $\delta\Gamma(\mathbf{r}_2,\mathbf{r}_1)$ can be found using the perturbative approach within the diffusion framework described in Appendix A. With the help of Eq. (19), we obtain

$$\delta\Gamma(\mathbf{r}_2,\mathbf{r}_1) \simeq \tilde{\mathcal{V}}^{\mathrm{I}}\frac{\tau}{\gamma}\,\Gamma(\mathbf{r}_2,\mathbf{r}_0)\,\Gamma(\mathbf{r}_0,\mathbf{r}_1), \tag{22}$$

where $\tilde{\mathcal{V}}^{\mathrm{I}} = -v_E k\epsilon''\delta V$ is the strength of the perturbation. Substituting Eq. (22) into Eq. (21), we obtain the change in flux in the form

$$\delta\overline{|\mathcal{R}_{ba}|^2} \simeq 4\tilde{\mathcal{V}}^{\mathrm{I}}\frac{\tau}{\gamma}\,J_b(\mathbf{r}_0)\,J_a(\mathbf{r}_0), \tag{23}$$

where we introduced a diffusive flux

$$J_a(\mathbf{r}_0) = k_a^z \int d\mathbf{r}_1\,\Gamma(\mathbf{r}_0,\mathbf{r}_1)\,\left|\langle\mathbf{r}_1|\overline{G}_0|\chi_a\rangle\right|^2. \tag{24}$$

This quantity is proportional to the mean intensity $\overline{I}_a(\mathbf{r}_0) \equiv \overline{|\phi_a(\mathbf{r}_0)|^2} = \overline{\left|2i\sqrt{k_a^z}\langle\mathbf{r}_0|G_0|\chi_a\rangle\right|^2}$ excited at $\mathbf{r}_0$ by the input channel $|\psi_a\rangle$. Unlike $\overline{G}_0$, the averaged modulus square of G_0 is described by diffusion and can be computed as

$$\begin{aligned}\overline{I}_a(\mathbf{r}_0) &= 4k_a^z\int d\mathbf{r}_1 d\mathbf{r}_2\,\left|\langle\mathbf{r}_0|\overline{G}_0|\mathbf{r}_2\rangle\right|^2\Gamma(\mathbf{r}_2,\mathbf{r}_1)\,\left|\langle\mathbf{r}_1|\overline{G}_0|\chi_a\rangle\right|^2\\ &\simeq 4k_a^z\int d\mathbf{r}_2\,\left|\langle\mathbf{r}_0|\overline{G}_0|\mathbf{r}_2\rangle\right|^2\int d\mathbf{r}_1\Gamma(\mathbf{r}_0,\mathbf{r}_1)\,\left|\langle\mathbf{r}_1|\overline{G}_0|\chi_a\rangle\right|^2\\ &= \frac{4}{\gamma}J_a(\mathbf{r}_0).\end{aligned} \tag{25}$$

Here, we used the fact that $\int d\mathbf{r}_2\left|\langle\mathbf{r}_0|\overline{G}_0|\mathbf{r}_2\rangle\right|^2 = -(\ell/k)\,\mathrm{Im}\langle\mathbf{r}_0|\overline{G}_0|\mathbf{r}_0\rangle$ and, from the definition of the mean density of states, $\mathrm{Im}\langle\mathbf{r}_0|\overline{G}_0|\mathbf{r}_0\rangle = -\pi c\,\mathrm{DOS}(\omega)/2k$. Combining now Eqs. (16), (23), and (25), we find the variation of the mean flux due to the perturbation

$$\delta\bar{F}_{\mathrm{diff}} \simeq \tilde{\mathcal{V}}^{\mathrm{I}}\frac{\tau\gamma}{4}\,\overline{I}_{\mathrm{in}}(\mathbf{r}_0)\,\overline{I}_{\mathrm{out}}(\mathbf{r}_0), \tag{26}$$

in terms of the intensities at position $\mathbf{r}_0$ excited from input and output (i.e., detector) ports

$$\begin{aligned}\overline{I}_{\mathrm{in}}(\mathbf{r}_0) &= \sum_{a=1}^{N_1}|v_a|^2\,\overline{I}_a(\mathbf{r}_0),\\ \overline{I}_{\mathrm{out}}(\mathbf{r}_0) &= \sum_{b=1}^{N_2}\overline{I}_b(\mathbf{r}_0).\end{aligned} \tag{27}$$

We note that the coefficients $|v_a|^2 \to 1$ if we can assume random and statistically equivalent excitation. Therefore, we will refer to these intensities as $\overline{I}^{\mathrm{RI}}_{\mathrm{in}}(\mathbf{r}_0)$, $\overline{I}^{\mathrm{RI}}_{\mathrm{out}}(\mathbf{r}_0)$ below, where RI again indicates random input.

To complete the derivation of the sensitivity $\overline{S}_{\mathrm{diff}} = d\bar{F}_{\mathrm{diff}}/d\epsilon''$ in the diffusive approximation, we substitute all prefactors into Eq. (26) and use the density of states $\mathrm{DOS}^{\mathrm{2D}}(\omega) = k/2\pi c$ or $\mathrm{DOS}^{\mathrm{3D}}(\omega) = k^2/2\pi^2 c$. We then obtain the main result of this section:

$$\overline{S}_{\mathrm{diff}}(\mathbf{r}_0) = -k^2\delta V\left(\frac{\pi}{k}\right)^{\mathcal{D}-2}\overline{I}^{\mathrm{RI}}_{\mathrm{in}}(\mathbf{r}_0)\,\overline{I}^{\mathrm{RI}}_{\mathrm{out}}(\mathbf{r}_0). \tag{28}$$

The coefficient in front of this expression depends on the dimensionality $\mathcal{D} = 2, 3$. This expression lends itself to an insightful physical interpretation. Indeed, $\overline{I}^{\mathrm{RI}}_{\mathrm{in}}(\mathbf{r}_0)$ is proportional to the probability of a photon injected at the input port reaching the localized perturbation at $\mathbf{r}_0$. Likewise, $\overline{I}^{\mathrm{RI}}_{\mathrm{out}}(\mathbf{r}_0)$ is proportional to the probability of a photon that passes through $\mathbf{r}_0$ reaching the output. Thus, Eq. (28) is, up to a prefactor, the conditional probability that a photon injected at the input will reach the output after having visited $\mathbf{r}_0$. For a half-space geometry, the spatial map described by the above expression is an arch, or "banana" [10,16,47,51,52], as it is commonly called.

We now turn to a comparison between the expression for optical sensitivity derived within the diffusion approximation [Eq. (28)] and the microscopic expression [Eq. (8)] obtained in Sec. II A. The microscopic formulation applies to a single realization of disorder and does not rely on statistical averaging or assumptions about large (relative to the transport mean free path) system sizes or source-detector separations. This generality allows it to capture both sample-specific and ensemble-averaged behavior for an arbitrary input state, whereas the diffusive result provides only the disorder-averaged sensitivity for a random input state. Therefore, we should expect that the macroscopic and diffusive descriptions both yield the same result when Eq. (8) is applied to a diffusive system and appropriately averaged. In the next subsection, we present a formal proof of this equivalence.

D. Microscopic sensitivity in the diffusive limit

In Sec. II A, we obtained the microscopic expression (9) for the optical sensitivity. For systems exhibiting diffuse wave transport, this formula should be equivalent, in the statistical sense, to the diffuse sensitivity given in Eq. (28). To verify this, we need to take the proper limit and account for the underlying assumptions. These include: (1) the characteristic size parameters of the system are sufficiently larger than the transport mean free path, justifying a diffusive treatment; (2) statistical averaging over an ensemble of disorder realizations; and (3) random excitation of the incident modes.

As the first step, we express the sensitivity in Eq. (9) in terms of the field Green's function. Using the Fisher-Lee relation (17), we obtain

$$\mathcal{S}(\mathbf{r}_0) = -8k^2\delta V \sum_{baa'} v_a^* v_{a'} k_b^z \sqrt{k_a^z k_{a'}^z}\, \mathrm{Im}\left[\langle\chi_b|G_0|\mathbf{r}_0\rangle\langle\mathbf{r}_0|G_0|\chi_{a'}\rangle\langle\chi_b|G_0|\chi_a\rangle^*\right]. \tag{29}$$

Likewise, the sensitivity in the diffusion approximation, Eq. (28), can be expressed in terms of the field Green's functions as

$$\overline{\mathcal{S}}_{\mathrm{diff}}(\mathbf{r}_0) = -16k^2\delta V \left(\frac{\pi}{k}\right)^{\mathcal{D}-2} \sum_{ba} |v_a|^2 k_b^z k_a^z\, \overline{|\langle\chi_b|G_0|\mathbf{r}_0\rangle|^2}\ \overline{|\langle\mathbf{r}_0|G_0|\chi_a\rangle|^2}. \tag{30}$$

Therefore, we seek a connection between Eqs. (29) and (30), provided we take advantage of the random-excitation assumption (3) and statistical averaging (2). The former gives $\overline{v_a^* v_{a'}} = \delta_{aa'}$, whereas the latter leads to the condition

$$\overline{\mathrm{Im}\left[\langle\chi_b|G_0|\mathbf{r}_0\rangle\langle\mathbf{r}_0|G_0|\chi_a\rangle\langle\chi_b|G_0|\psi_a\rangle^*\right]} = 2\left(\frac{\pi}{k}\right)^{\mathcal{D}-2} \overline{|\langle\chi_b|G_0|\mathbf{r}_0\rangle|^2}\ \overline{|\langle\mathbf{r}_0|G_0|\chi_a\rangle|^2} \tag{31}$$

for the mean of Eq. (29) to be equal to Eq. (30). In Appendix B, we use a diagrammatic approach to prove that the equality (31) indeed holds. This result can be qualitatively understood by considering the scattering paths that contribute the most after disorder averaging. These dominant scattering paths consist of diffusive trajectories, as shown in Fig. 2. Consequently, we have established that under random illumination, the statistically averaged microscopic sensitivity, Eq. (8), and diffusive intensity sensitivity, Eq. (28), yield identical results.

We note that when the illumination is not random but remains independent of the disorder, this equivalence is still often preserved. For instance, it holds for a simple plane-wave input ($v_a = \delta_{a,a_0}$), since in this case $v_a^* v_{a'} = \delta_{a,a'}$ trivially. It also holds for input states with a large number of nonzero coefficients v_a that are uncorrelated with the medium, because the cross terms ($a \neq a'$) in Eq. (29) acquire random phase-dependent weights that are washed out upon summation.

This derivation above also exposes the mechanism by which the relationship between Eqs. (8) and (28) can be broken. Indeed, choosing the v_a coefficients dependent on the specific realization of disorder would make them dependent on the Green's function matrix elements in Eq. (29), thereby preventing the factorization of disorder averages and rendering Eq. (28) no longer applicable. This is precisely the effect of coherent excitation—choosing an incident wavefront uniquely tailored to the specific disorder realization, as explored in Secs. III and IV B.

E. From extensive to intensive optical sensitivity

Earlier in this section, we derived two expressions for computing sensitivity: a microscopic formulation, Eq. (8), and its diffusive approximation, Eq. (28). These expressions allow us to identify several key properties of sensitivity, which, by definition, is given by the ratio of

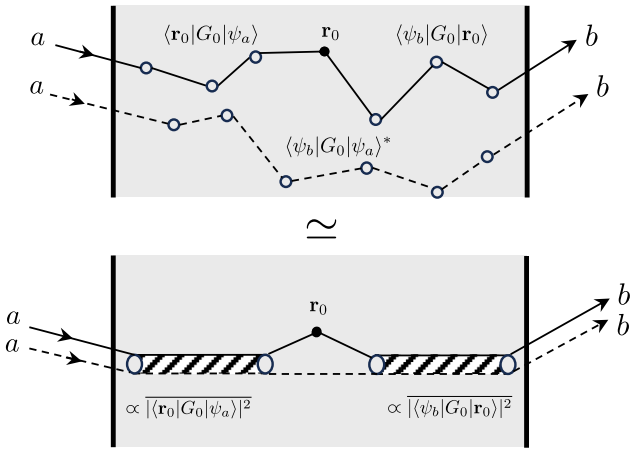

FIG. 2. Scattering representation of the identity (31). Solid and dashed lines represent the propagating field and its complex conjugate, while open circles represent scatterers. Shaded tubes represent diffusive paths where both fields visit the same scatterers. A more formal representation of the lower diagram is given in Appendix B.

flux variation to the magnitude of the perturbation in the imaginary part of the dielectric function.

Volume of perturbation: The spatial dependence of the absorbing center has been modeled by a delta function [see Eq. (3)]. This assumption implies that the spatial extent of the perturbation $\delta V^{1/\mathcal{D}}$ is much smaller than the characteristic spatial variation scale of the field. In the microscopic formulation, Eq. (8), which applies to a single realization of disorder, the relevant length scale is the optical wavelength $\lambda = 2\pi/k$ since interference effects govern the field structure. Although the structural correlation length (e.g., cell size) may be larger than λ, it does not limit the field resolution, and a conservative validity condition is still $\delta V^{1/\mathcal{D}} \ll \lambda$. In contrast, after statistical averaging—as in the diffusive expression, Eq. (28)—both the wavelength and correlation length become irrelevant. The spatial variations in the averaged fields are smoothed over the transport mean free path ℓ, which sets the smallest relevant scale. Thus, in the diffusive regime, the delta-function approximation remains valid provided that $\delta V \ll \ell^{\mathcal{D}}$ [see Eq. (A5) in Appendix A]. Therefore, weakness of perturbation amounts to the condition $k^{\mathcal{D}}\,\delta V \delta\epsilon \ll 1$ (c.f. Eqs. (3) and (A5)), making both Eq. (8) and its diffusive approximation Eq. (28) trivially dependent on δV. As such, sensitivity becomes an extensive quantity—it scales with the size of the perturbation. In contrast, an intensive definition would normalize away this dependence making it "density"-like. Therefore, we propose normalization by the dimensionless quantity $k^{\mathcal{D}}\,\delta V$ (see below).

Number of input spatial channels: In Secs. II A and II C, we adopted such a normalization that, on average, a unit of flux is incident onto each of N_1 degrees of freedom in the input port. This is a "constant intensity" normalization—it leads to the total flux being proportional to the *area* of the injection site and, thus, to N_1 itself. In other words, the sensitivity is trivially dependent on N_1, again, making it an extensive property and suggesting a natural normalization by N_1.

Number of output spatial channels: The change in flux collected at the output should similarly increase with the collection area, or N_2, the number of degrees of freedom at the output port. In the diffusive approximation, Eq. (28), the proportionality should be nearly linear, provided that the size of the port is much smaller than the transport mean free path. Similar to the two other dependencies discussed above, normalization by N_2 appears natural.

Based on the arguments above, we introduce a normalized optical sensitivity defined as

$$\mathfrak{s}(\mathbf{r}_0) \equiv \frac{\mathcal{S}(\mathbf{r}_0)}{k^{\mathcal{D}}\,\delta V N_1 N_2}. \tag{32}$$

Such a normalization in both Eqs. (8) and (28) defines the sensitivity density. While this removes the dependence on the perturbation volume, it does not eliminate the dependence on other system parameters such as N_1, N_2, or geometry (c.f. Sec. III D). Nevertheless, the sensitivity density is particularly convenient when comparing different models or simulations—the task we undertake in the next section.

III. NUMERICAL ANALYSIS: SCALAR WAVES

In the previous section, we introduced the microscopic expression for optical sensitivity Eq. (8) and its diffusion approximation Eq. (28). Instead of sequential raster scanning the location of the absorbing center [Fig. 3(a)] to map out the sensitivity, both formulations have the major advantage of being "parallel." Indeed, Eq. (8) expresses the entire sensitivity map in terms of two fields $E_0(\mathbf{r})$ and $\phi(\mathbf{r})$, requiring only two computations for each disorder configuration [Fig. 3(b)] followed by ensemble averaging. Equation (28), on the other hand, relates the sensitivity map to the ensemble-averaged intensity distributions for input and output ports. In Sec. II D, we showed that both formulations should agree in a diffusive system with random input excitation. In Sec. III B, we aim to verify that both Eqs. (8) and (28) indeed give the same result in this limit in numerical simulation of scalar waves in the two-dimensional (2D) semi-infinite medium introduced in Sec. III A. This is not a trivial test because the quantities and the averaging procedure in the two expressions are vastly different. Next, in Sec. III C we show that under excitation with a disorder-specific wavefront, the maximum remission eigenchannel, the diffusive approximation fails to describe the optical sensitivity computed using our microscopically exact Eq. (8). We also demonstrate that the sensitivity for the remission eigenchannel can be

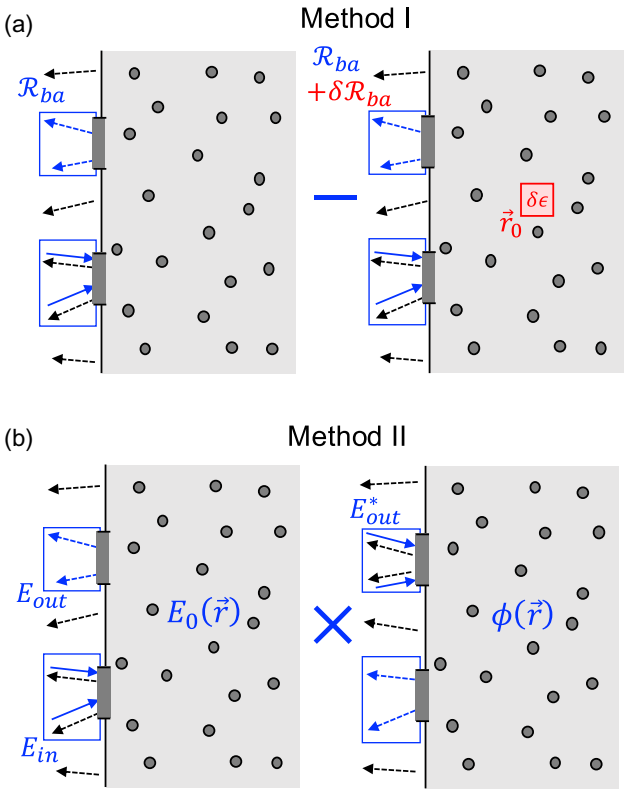

FIG. 3. Two computational approaches for evaluating optical sensitivity. (a) Method I: sensitivity is inferred from changes in remission coefficients $\mathcal{R}_{ba}$ due to the introduction of a *localized absorber* at position $\mathbf{r}_0$ [see first part of Eq. (8)]. This method requires sequential simulations for each $\mathbf{r}_0$ and thus involves raster scanning. (b) Method II: sensitivity is computed using the product of two field distributions in the second part of Eq. (8). This approach is parallel and requires only two simulations to obtain the full spatial sensitivity map across all $\mathbf{r}_0$.

predicted by the filtered random matrix theory summarized in Appendix G. In Sec. III D we discuss relationship between enhancement of sensitivity and the remission enhancement.

A. Numerical model

We carry out our numerical simulations in a geometry chosen to represent the experimental sample from our previous work [32]. The system is a 2D disordered medium occupying a half-space, as shown in Fig. 3. This 2D configuration is not arbitrary: it models a planar photonic structure in the experiment, which enables nearly noninvasive optical access to the internal field distribution [53], making it ideally suited to studying coherent wave transport *inside* a multiple scattering medium. The electromagnetic waves in such structures are effectively confined in the vertical (out-of-plane) direction [29,54–56], with radiative leakage inhibited by total internal reflection due to the refractive index difference with surrounding media [57,58] (air and substrate). This indeed allows a reduction to a 2D model, in which electromagnetic fields decouple into two independent polarizations: transverse magnetic (TM) and transverse electric (TE) [59,60]. TM polarization corresponds to one out-of-plane electric field component and two in-plane magnetic field components, while TE polarization involves two in-plane electric field components and one out-of-plane magnetic field component. Waves with TM and TE polarizations propagate independently in 2D. Crucially, since scattering arises through the electric field, the interaction with disorder due to randomly varying dielectric permittivity differs: TM waves couple via a single electric field component, while TE waves involve two, leading to fundamentally different scattering behavior.

In this section, we consider TM polarization, which obeys a scalar wave equation [49] corresponding to Eq. (1). This choice is consistent with the modeling approach in Ref. [32], where numerical simulations were performed using the KWANT package [61]. Here, we employ the MESTI (Maxwell's Equations Solver with Thousands of Inputs) software package [62], which offers a substantial computational speedup through an augmented partial factorization method. In this work, we do not consider spatially uniform loss, which would be required to simulate the effects of weak out-of-plane scattering in experiments [32]. In our previous work [63], MESTI was validated against KWANT and shown to produce quantitatively consistent results. In Sec. IV B, we extend our study to TE polarization using MESTI's vector-wave capabilities, allowing further verification of the microscopic approach to optical sensitivity, thereby validating and extending the applicability of the microscopic sensitivity model to vector waves involving multiple polarization components.

Based on the above considerations, we conduct 2D simulations with the following parameters: vacuum wavelength $\lambda_0 = 1.55$ μm, slab dimensions $L \times W = 250 \times 300$ μm^2, and background refractive index $n_{\text{eff}} = 2.85$. Disorder is introduced by placing a low concentration of circular air holes—filling fraction $f = 10\%$, radius $a = 100$ nm, and refractive index $n_{\text{air}} = 1$. These parameters were chosen to ensure that the diffusion approximation is satisfied, i.e., $\ell \ll W, L$. This condition also guarantees that the sample thickness greatly exceeds the input-output separation, so the medium can be regarded as effectively semi-infinite. The actual value of $\ell = 6.4$ μm was matched to the experiment in Ref. [32], but this is irrelevant in the context of the current discussion. The value of ℓ has been determined using the procedure described in Ref. [63]. We will also present the results of simulations where the transport mean free path is varied. To model the effect of open boundaries, the numerical domain was surrounded by a perfectly matched layer [59]. Injection and detection ports of widths W_1 and W_2, separated by distance $d \gg \ell$, are modeled by attaching two waveguides to the

front interface (see Fig. 3). We will present simulations for different combinations of these parameters.

We finally note that while all 2D disordered systems are expected to exhibit Anderson localization effects [33], these only become relevant at lengths comparable to or exceeding the localization length ξ. In the weak-scattering regime considered here ($k\ell \gg 1$), this length is exponentially large, $\xi \propto \ell \exp(c\,k\ell)$ with $c \sim 1$ [33]. For the parameters used in our simulations, as well as in typical optical experiments, ξ is vastly larger than the system size and all other relevant scales, so localization effects can be safely neglected.

B. Random input excitation

Computing optical sensitivity using Eq. (8) requires knowledge of two fields: $E_0(\mathbf{r}_0)$ and $\phi(\mathbf{r}_0)$. The former is the field inside the system obtained by illuminating it through the input port with a random combination of all modes. Computing the latter field requires a separate simulation, but for the same configuration of disorder. This is obtained by recording the field at the output port from the first simulation, conjugating it, and sending it back into the sample as the input for the second simulation. Having computed the internal fields, the quantity in Eq. (8) is obtained for that specific disorder configuration. Subsequently, we compute this expression for 1000 realizations of disorder, requiring twice as many simulations to achieve a sufficient statistical average. Figure 4(a) depicts the result found for a system with $\ell = 6.4\ \mu$m, $W_1 = W_2 = 10\ \mu$m, and an input-output separation of $d = 128\ \mu\text{m} = 20 \times \ell$. The characteristic "banana" shape can be seen. We would like to emphasize again the remarkable fact that the statistical average of the product of two *fields* in Eq. (8) results in a nonzero value.

Computations based on Eq. (28) require statistically averaged intensities throughout the volume of the system. These are obtained by illuminating it through input port with a random combination of all modes. Thus, the simulations used to compute $E_0(\mathbf{r}_0)$ for Eq. (8) can be reused to compute $\bar{I}^{\text{RI}}_{\text{out}}(\mathbf{r}_0)$—this is obtained by a mirror reflection across the horizontal line through the middle of the system.

In Fig. 4(b), we compare the sensitivities computed from Eqs. (8) and (28)—circles and crosses, respectively—and normalized via Eq. (32). Here, the separation distance is fixed at $d = 128\ \mu\text{m} = 20 \times \ell$, and multiple values $W_1 = W_2$ are tested. We can see that, as expected based on the theoretical argument in Sec. II D, the two methods give the same result. The fact that simulations for different values of $W_1 = W_2$ agree among themselves also supports our argument in Sec. II E for normalizing sensitivities. Furthermore, in Appendix C, we demonstrate that the curves in Fig. 4(b) agree with simulations performed for $W_1 \neq W_2$ cases. Such an agreement is also expected for the normalized sensitivities, based on Eq. (32).

In Fig. 4(c), we demonstrate that the dependence on the input-output separation d can also be predicted by

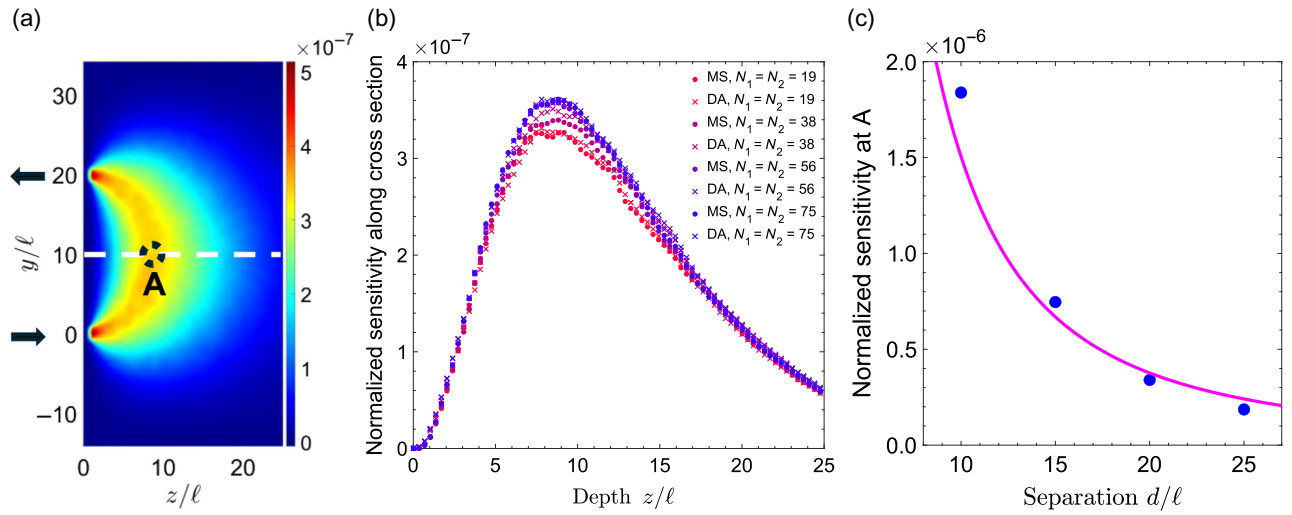

FIG. 4. Comparison of microscopic and diffusive models for optical sensitivity under random input excitation. All results are averaged over 1000 disorder realizations and normalized according to Eq. (32). The transport mean free path is $\ell = 6.4\ \mu$m. (a) Sensitivity map computed using the microscopic sensitivity (MS) expression, Eq. (8), exhibits the characteristic banana-shaped pattern. The input and output port widths are $W_1 = W_2 = 10\ \mu$m; the source-detector separation is $d = 128\ \mu\text{m} = 20 \times \ell$. (b) Depth cross section of the sensitivity map along the dashed line in (a). Circles correspond to the MS calculation [Eq. (8)]; crosses show results from the diffusion approximation (DA) [Eq. (28)]. The input and detector port widths are equal. Curves are shown for 5, 10, 15, and 20 μm, with fixed separation $d = 128\ \mu\text{m} = 20 \times \ell$. (c) Sensitivity at the midpoint A of the banana [peak in panel (b)] as a function of source-detector separation. Symbols: MS results using Eq. (8) for $W_1 = W_2 = 10\ \mu$m; solid line: DA prediction based on analytic intensity profiles substituted into Eq. (28), as described in Appendix D.

substituting analytical solutions for $\bar{I}_{\text{in}}^{\text{RI}}(\mathbf{r}_0)$ and $\bar{I}_{\text{out}}^{\text{RI}}(\mathbf{r}_0)$ found from the diffusion equation. We derive such a solution in Appendix D. The decrease in the sensitivity $\bar{\mathcal{S}}_{\text{diff}} \simeq -1/(\pi^2 k^2 d^2) \propto 1/d^2$ with increasing d is the well-known trade-off between depth and sensitivity. Indeed, larger d leads to an increase in the radius of the banana pattern in the sensitivity map. Photons undergoing diffusive random walks along these long paths are less likely to reach the output port. As a consequence, the remitted signal is less sensitive to the total flux variation due to local perturbation at larger depth inside the system [see Fig. 4(c)].

For completeness, we computed sensitivity using a brute-force sequential approach—Method I—in Fig. 3(a). Recall that sensitivity is defined as $\mathcal{S}(\mathbf{r}_0) = \delta F/\delta\epsilon''$—the difference between the average remitted flux detected at the output waveguide with and without a perturbation center at $\mathbf{r}_0$. The agreement with Eq. (8), shown in Appendix D, provides further evidence for the robustness of our microscopical approach to optical sensitivity.

C. Shaped-wavefront excitation

We motivate this section by revisiting the assumptions used in obtaining Eq. (28)—the diffusion approximation for optical sensitivity. In fact, this incorporates two separate assumptions that become particularly clear when we examine the process of averaging in the microscopically exact Eq. (9). The first assumption is the diffusion approximation itself, stating that the ensemble-averaged intensities can be described by the diffusion equation and that the dimensions of the system are much larger than the transport mean free path. The second assumption has to do with the averaging procedure of the input wavefront encoded by coefficients v_a in Eq. (9). The procedure involved in obtaining Eq. (28) in Sec. II C amounts to performing disorder averaging with no regard for the values of v_a. Therefore, once the diffusion approximation has been made, it is no longer possible to account for a specific input wavefront. This observation motivates the use of the microscopic expression for sensitivity, Eq. (8) [equivalent to Eq. (9)], including the sample-specific excitation coefficients, and only then performing statistical averaging.

Second, it has been shown in Ref. [32] that by exciting the system with an incident wavefront corresponding to the MRE [see the description before Eq. (14)], we could enhance not only the signal in remission but also the sensitivity. In our previous work, we used the proper microscopical expression Eq. (8) to compute the sensitivity; however, it remained unclear whether Eq. (28) could still apply with $\bar{I}_{\text{in}}^{\text{MRE}}(\mathbf{r}_0)$ and $\bar{I}_{\text{out}}^{\text{MRE}}(\mathbf{r}_0)$ substituted instead of intensities for random input excitation. Below, we clearly demonstrate that Eq. (28) is *inadequate and cannot be used* to describe the optical sensitivity of remission eigenchannels.

Here, we carry out comprehensive numerical tests of the results of Sec. II C. Figure 5(a) shows the disorder-averaged microscopic sensitivity (MS) map in Eq. (8), computed for the MRE for a system with $W_1 = W_2 =$ 10 μm, separation $d = 20 \times \ell$, and transport mean free path $\ell = 6.4$ μm. We observe, in agreement with our earlier work [32], that the sensitivity map retains the banana shape but is enhanced by a factor that appears to be constant within the accuracy of our simulation. Remarkably, as we verify in Appendix C, this conclusion holds even when $W_1 \neq W_2$. Therefore, below, we present only the depth dependence of the sensitivity maps taken along the line $y = d/2$, shown as the dashed line in Fig. 5(a).

In Fig. 5(b), we compare the sensitivity maps for MRE excitation obtained using two different methods. The filled circles represent numerical results computed using the microscopically exact Eq. (8), which remains valid for coherent excitation. The crosses, however, require careful interpretation. While Eq. (28) (derived in the diffusion approximation) is rigorously justified for random input excitation, it does not strictly apply to the coherently excited MREs for two reasons. First, as noted above, averaging of intensities cannot be carried out separately from averaging of the excitation coefficients v_a, which are unique to each disorder realization. Second, the diffusion equation does not accurately describe the disorder-averaged intensity distribution of MREs due to interference effects, which are neglected in the diffusion approach. Nevertheless, as an exploratory step, we substitute the numerically computed disorder-averaged intensity of MREs into Eq. (28), yielding the results represented by the crosses. While this substitution lacks theoretical justification, it provides an empirical comparison and helps assess the limitations of the diffusion approximation in this context. To avoid confusion, we denote these data as DA* rather than DA, emphasizing that they are not a direct application of the diffusion approximation but rather an *ad hoc* extension.

Among the four datasets, corresponding to $W_1 = W_2 =$ 5, 10, 15, and 20 μm, DA* agrees with the MS in only one case. We believe this agreement is accidental. To simplify the analysis, we limit our discussion to the value of sensitivity in the middle of the banana, labeled with the letter "B" in Fig. 5(a). Since we have already determined that the sensitivity maps retain their shape, comparison of its value at a predetermined point is sufficient. In Figs. 5(c)–5(f), we tested whether DA* is capable of describing MS when the parameters d, ℓ, N_1, and N_2 are varied. We conclude that, in sharp contrast to the applicability of DA to the random input case in Fig. 4, DA* is inadequate in describing the MS of the MRE. In other words, the sensitivity in the case of controlled wavefront excitation does not reduce to a product of two intensities as in Eq. (28). This systematic deviation between MS and DA* provides direct evidence of nontrivial correlation effects, which are neglected when

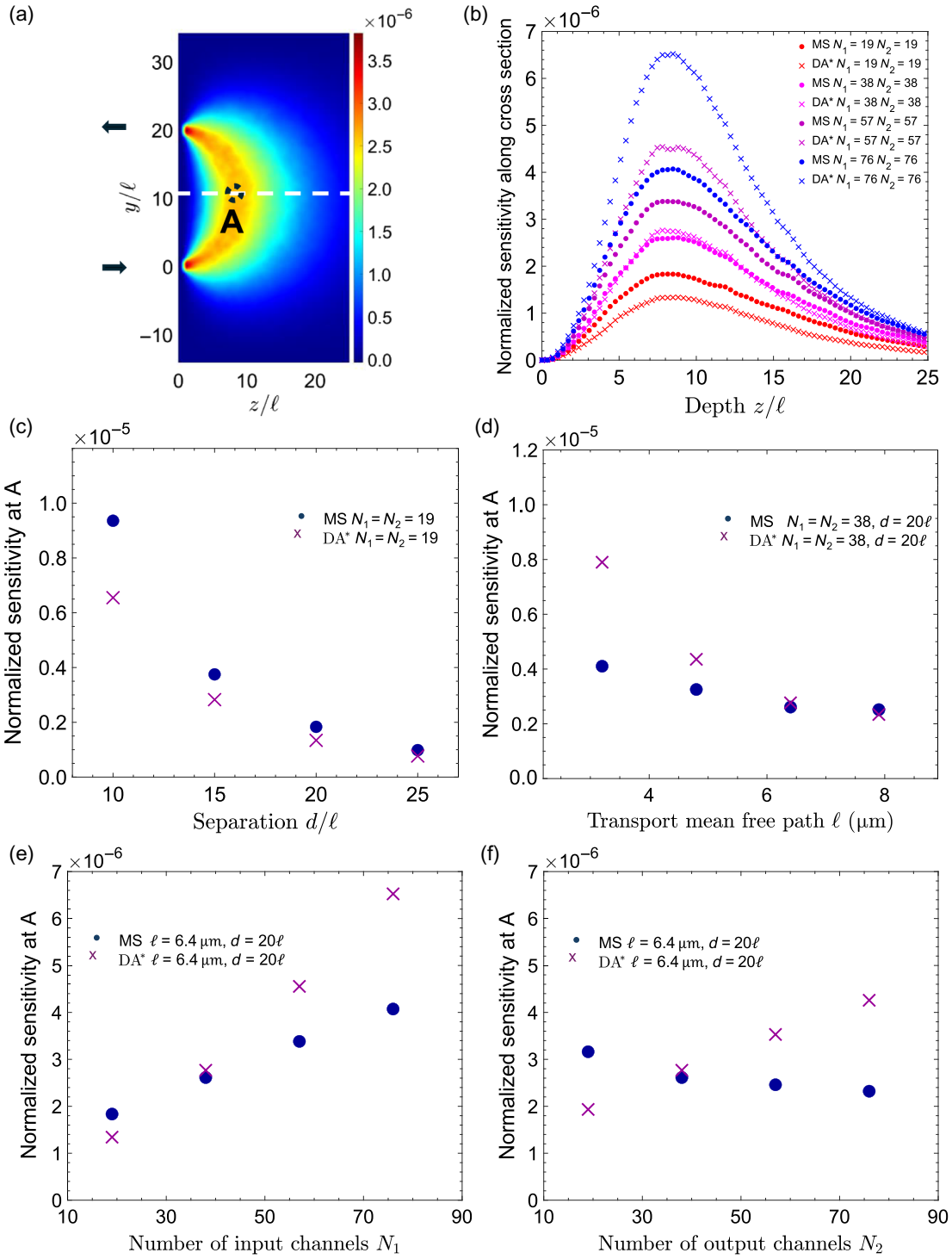

FIG. 5. Sensitivity map for excitation with the maximum remission eigenchannel (MRE) and comparison with diffusion-based predictions. (a) Sensitivity map computed using the microscopically exact expression, Eq. (8), for MRE excitation. The characteristic banana-shaped pattern is preserved, but the overall sensitivity is enhanced compared to the random input case. Parameters: $W_1 = W_2 = 10\ \mu$m, the separation is $d = 20 \times \ell$, and the transport mean free path $\ell = 6.4\ \mu$m. (b) Depth cross section along the midplane [dashed line in panel (a)], comparing sensitivity from the MS formulation [Eq. (8), filled circles] and a heuristic application of Eq. (28) using the disorder-averaged intensity of MREs (crosses, denoted as DA*); see main text for details. (c)–(f) Sensitivity at the central point A in panel (a), plotted as a function of: (c) input-output separation d; (d) transport mean free path ℓ; (e) number of input channels N_1, and (f) number of output channels N_2. In all cases, the results are averaged over 1000 disorder realizations and normalized according to Eq. (32).

statistical averaging over input field patterns is performed separately from intensities in Eq. (9).

D. Relationship between sensitivity enhancement and remission enhancement

In our previous work [32], we observed the intriguing result that the enhancement of sensitivity $\eta_{\mathcal{S}}^{\mathrm{MRE}}$ was close to the enhancement of the remission $\eta_{\mathcal{R}}^{\mathrm{MRE}}$ for the MRE. If generally true, such a relationship could be extremely useful because the enhancement of remission can be theoretically predicted. Indeed, the theoretical technique [64–66] called filtered random matrix (FRM) theory has been shown to correctly reproduce the full distributions of the eigenvalues of a subset of the full scattering matrix of a complex system, in our case $\mathcal{R}$. In Ref. [32], we used FRM theory to obtain an analytical expression for the remission enhancement—the ratio $\rho_{\max}/\bar{\rho} = \eta_{\mathcal{R}}^{\mathrm{MRE}}$ between the maximum and average eigenvalues of the remission matrix $\mathcal{R}^{\dagger}\mathcal{R}$. In Appendix G, we include a brief summary of FRM theory. A less accurate but more intuitive model—the effective Marchenko-Pastur model—is also presented in Appendix H.

In Figs. 6(a)–6(d), we compare theoretical predictions for the remission enhancement $\eta_{\mathcal{R}}^{\mathrm{MRE}}$ to the sensitivity enhancement $\eta_{\mathcal{S}}^{\mathrm{MRE}}$ and find that they indeed agree well. We now present an argument that this relationship is related to the invariance of the sensitivity map to the input field profile, as observed in Sec. III C above.

Let us recall that, by definition, the sensitivity is the response of the flux to the *localized* perturbation $\delta\epsilon(\mathbf{r}) = i\epsilon''\delta(\mathbf{r}-\mathbf{r}_0)$: $\mathcal{S}(\mathbf{r}_0) = \delta F(\mathbf{r}_0)/\epsilon''$ [see Eq. (8)]. As such, $\delta F(\mathbf{r}_0)$ implicitly depends on the location of the perturbation. By performing volume integration over $\mathbf{r}_0$ on both

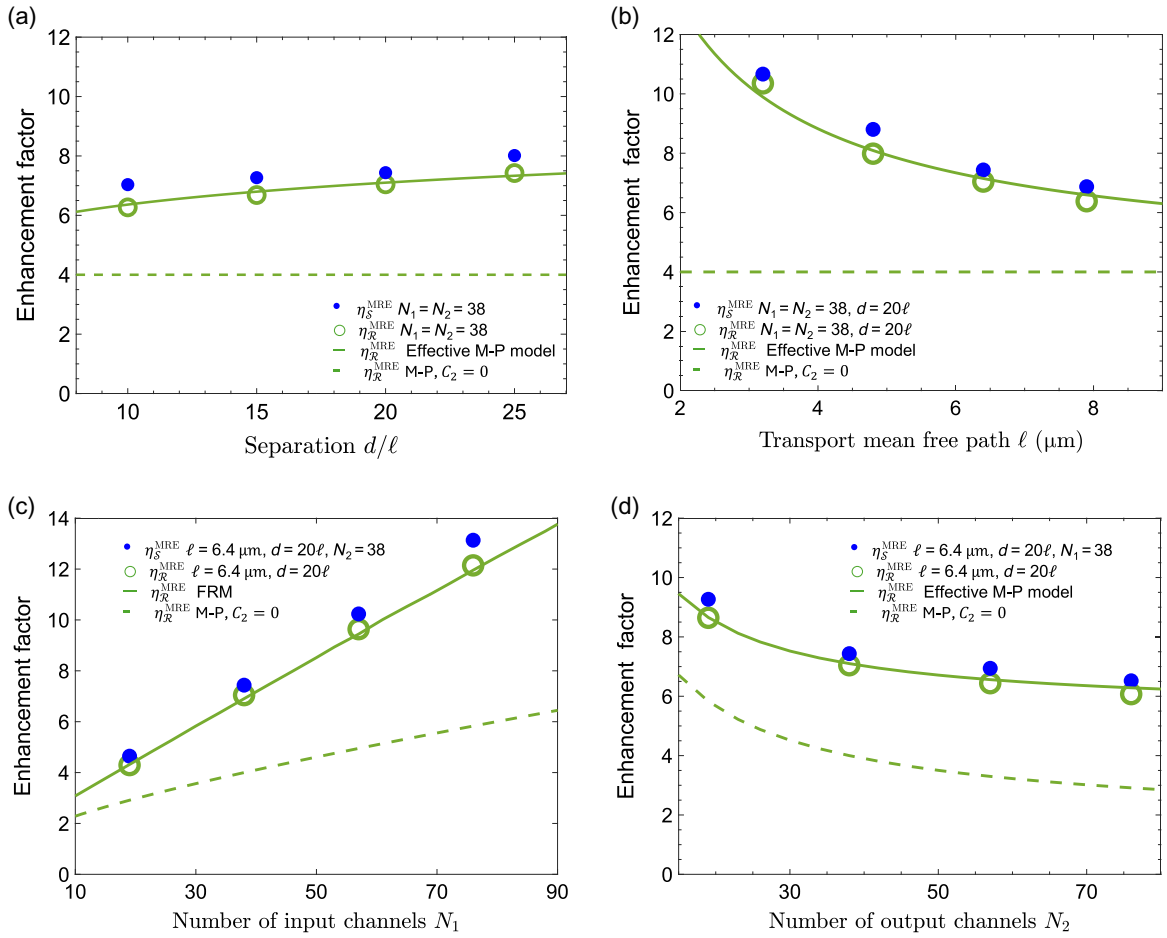

FIG. 6. Comparison between remission and sensitivity enhancement factors. (a)–(d) Symbols show the enhancement factors for sensitivity $\eta_{\mathcal{S}}^{\mathrm{MRE}}$ (filled circles) and remission $\eta_{\mathcal{R}}^{\mathrm{MRE}}$ (open circles) as a function of (a) source-detector separation d, (b) transport mean free path ℓ, (c) input-port width W_1, and (d) output-port width W_2; see text for definitions. Solid lines in panels (a), (b), and (d) represent predictions from the effective Marchenko-Pastur (MP) model [see Eq. (H1) in Appendix H]. In panel (c), the solid line includes higher-order corrections based on filtered random matrix (FRM) theory, as described in Appendix G [Eq. (G17)]. Dashed lines correspond to the MP-model prediction when the contribution of long-range correlations C_2 is omitted [Eq. (38)].

sides of the definition of sensitivity, we conclude that

$$\int \mathcal{S}(\mathbf{r}_0)d^3\mathbf{r}_0 \propto \int \delta F(\mathbf{r}_0)d^3\mathbf{r}_0. \tag{33}$$

Volume integration of the localized perturbation is equivalent to estimating sensitivity to a global, i.e., spatially uniform, perturbation ϵ''. We now assume that the volume-integrated change in flux, the right-hand side in Eq. (33), is proportional to the total flux without perturbation:

$$\int \mathcal{S}(\mathbf{r}_0)d^3\mathbf{r}_0 \propto \left[\sum_{baa'} \mathcal{R}^*_{a'b}\mathcal{R}_{ba}v^*_{a'}v_a\right], \tag{34}$$

where we used the explicit expression for the flux in terms of $\mathcal{R}$. This amounts to assuming that a sufficiently small uniform perturbation should reduce all elements of the remission matrix equally. This assumption is supported by theoretical and numerical studies showing that, in the weak-absorption regime, uniform loss preserves the spatial profiles of individual quasimodes and consequently attenuates all scattering coefficients proportionally [67,68].

Substituting appropriate input vectors v_a and performing statistical averages, we can find two versions of Eq. (34): one for the MRE and one for random input excitation. Forming a ratio, we obtain an insightful constraint

$$\frac{\int \overline{\mathcal{S}}^{\mathrm{MRE}}(\mathbf{r}_0)d^3\mathbf{r}_0}{\int \overline{\mathcal{S}}^{\mathrm{RI}}(\mathbf{r}_0)d^3\mathbf{r}_0} \approx \frac{\bar{\rho}_{\max}}{\bar{\rho}} \equiv \eta_{\mathcal{R}}^{\mathrm{MRE}}. \tag{35}$$

Here, we note that random input excitation is statistically equivalent to exciting each eigenchannel with equal probability, $\rho_{\mathrm{RI}} \equiv \bar{\rho}$, where $\bar{\rho}$ is the average remission eigenvalue. Such a relationship has profound implications—it states that the maximum achievable *global* (i.e., volume-integrated) enhancement of sensitivity is equal to the remission enhancement for the MRE:

$$\frac{\int \overline{\mathcal{S}}(\mathbf{r}_0)d^3\mathbf{r}_0}{\int \overline{\mathcal{S}}^{\mathrm{RI}}(\mathbf{r}_0)d^3\mathbf{r}_0} \leq \eta_{\mathcal{R}}^{\mathrm{MRE}}. \tag{36}$$

Wavefront shaping takes advantage of the linearity of the wave equation and is known to produce nontrivial constraints or sum rules [69].

Furthermore, the fact that the spatial distribution (the map) of sensitivity for the MRE is nearly the same as that for random input excitation, $\overline{\mathcal{S}}^{\mathrm{MRE}}(\mathbf{r}_0) \propto \overline{\mathcal{S}}^{\mathrm{RI}}(\mathbf{r}_0)$ [see Sec. III C], allows us to take the argument in Eq. (35) a step further and conclude that

$$\eta_{\mathcal{S}}^{\mathrm{MRE}} \simeq \eta_{\mathcal{R}}^{\mathrm{MRE}}. \tag{37}$$

This is an interesting result in the context of our discussion in Sec. II B, where we found that $\mathcal{S}^{\mathrm{PC}}$ yields the highest *local* sensitivity enhancement. The argument above now allows us to conclude that MRE achieves the highest *global* enhancement of sensitivity.

In Ref. [32], we observed that the discrepancy between $\eta_{\mathcal{S}}^{\mathrm{MRE}}$ and $\eta_{\mathcal{R}}^{\mathrm{MRE}}$ diminishes in the limit $d \gg W_1 + W_2$, which is fully consistent with our extensive tests of this relationship reported in Fig. 6. In fact, we see good agreement between sensitivity and remission enhancements for d as small as around $3 \times (W_1 + W_2)$ [Fig. 6(a)]. In Appendix H, we provide extensive numerical evidence relating $\eta_{\mathcal{S}}^{\mathrm{MRE}}$ to $\eta_{\mathcal{R}}^{\mathrm{MRE}}$.

The results presented in this section focus on 2D disordered systems, where the long-range intensity correlation of speckle patterns, usually denoted as C_2, contributes significantly to the remission enhancement (see Appendix G); however, in most three-dimensional (3D) diffusive media, particularly biological tissues, the impact of C_2 is expected to be considerably smaller, as its contribution to the enhancement, N_1C_2, scales as $\propto N_1/k\ell$ in 2D and as $\propto \sqrt{N_1}/k\ell$ in 3D. Consequently, in 3D media with $k\ell \gg 1$, the enhancement of optical sensitivity will primarily follow the prediction

$$\eta_{\mathcal{R}}^{\mathrm{MRE}} \xrightarrow[C_2 \to 0]{} \left(1 + \sqrt{\frac{N_1}{N_2}}\right)^2, \tag{38}$$

which stems from the Marchenko-Pastur limiting distribution for remission eigenvalues [32]. The dashed lines in Fig. 6 illustrate this limiting behavior by omitting the C_2 contribution from the sensitivity calculations. These results indicate that, although WFS in 2D can exploit mesoscopic correlations to enhance sensitivity beyond diffusion theory, enhancement of remission, and thus sensitivity, can also be achieved in 3D, particularly in the $N_1 \gg N_2$ regime. The physical mechanism for enhancement of remission and/or sensitivity in the absence of appreciable C_2 correlations is interference of multiple coherent contributions at the output port—a consequence of the determinism of wave transport.

IV. OPTICAL SENSITIVITY: VECTOR WAVES

Our previous theoretical and numerical analyses in Secs. II and III have been based on the scalar wave equation—Eq. (1). Although the scalar wave approximation is a common simplification in the study of wave transport in random media [49], its validity requires careful consideration in the context of coherent control via WFS. Indeed, it has been demonstrated that the polarization of the wave in strongly scattering media can reliably be manipulated [70,71]. Notably, the first step toward the full 3D vector-wave treatment can be readily made in 2D. In this geometry, the electromagnetic wave equation decouples into TM and TE polarization states. The former is equivalent to the 2D scalar wave equation, which we modeled numerically in Sec. III. TE polarization, on

the other hand, consists of two components of the electric field. Therefore, modeling TE waves incorporates an additional scattering channel, compared to scalar or TM waves, between the two polarization components of the electric field. In Ref. [63], we used numerical simulations to investigate whether wave polarization has any effect on the full distribution of the remission eigenvalues. We found that the distribution remained independent of the polarization provided that the two systems had the same macroscopical scattering parameters, i.e., the same transport mean free path. This is consistent with a recent numerical study [72], which found that the distribution of the transmission eigenvalues in fully vectorial 3D simulations coincides with that for scalar waves.

Generalizing this result to the sensitivity is far from obvious. Clearly, the sensitivity for scalar waves in Eq. (8) is determined by the interference between two fields—one launched from the input port $E_0(\mathbf{r}_0)$ and the other from the output one $\phi(\mathbf{r}_0)$. Extending such a formula to TE waves should, in fact, include interference effects between two polarization states of each field. Such a generalization is nontrivial, motivating us to revisit the derivation of sensitivity for TE waves below.

A. Mapping onto the scalar sensitivity model

We begin by enumerating the underlying assumptions of our theoretical model. First, we consider a TE-polarized wave propagating into a 2D scattering system. This corresponds to considering two in-plane components (x, y) of the electric field and one (z) component of the magnetic field. Second, we consider nonmagnetic media where $\mu \equiv \mu_0$. Lastly, scattering originates from the spatially nonuniform dielectric permittivity $\epsilon(\mathbf{r})$, which is assumed to be real. Under these conditions, the equation describing the out-of-plane component of the magnetic field $H_z(\mathbf{r})$ becomes

$$\nabla^2 H_z(\mathbf{r}) + k^2 \epsilon(\mathbf{r})\, H_z(\mathbf{r}) - \frac{1}{\epsilon(\mathbf{r})} \nabla\epsilon(\mathbf{r}) \cdot \nabla H_z(\mathbf{r}) = 0. \tag{39}$$

In contrast to the scalar case (TM polarization) in Eq. (1), we gain an additional term $\sim \nabla\epsilon(\mathbf{r}) \cdot \nabla H_z(\mathbf{r})$. Both vector quantities in this term lie in the plane.

In the next step, we demonstrate that it is possible, with a judicious change of variables, to transform Eq. (39) into a Helmholtz equation similar to Eq. (1) for scalar waves. Introducing the (scalar) function

$$h(\mathbf{r}) = \frac{H_z(\mathbf{r})}{\sqrt{\epsilon(\mathbf{r})}}, \tag{40}$$

we transform Eq. (39) into

$$\nabla^2 h(\mathbf{r}) + \kappa^2(\mathbf{r})\, h(\mathbf{r}) = 0, \tag{41}$$

where $\kappa^2(\mathbf{r})$ differs markedly from $k^2\epsilon(\mathbf{r})$ in Eq. (1),

$$\kappa^2(\mathbf{r}) \equiv k^2\, \epsilon(\mathbf{r}) + \frac{\nabla^2\epsilon(\mathbf{r})}{2\,\epsilon(\mathbf{r})} - \frac{3}{4}\frac{\nabla\epsilon(\mathbf{r}) \cdot \nabla\epsilon(\mathbf{r})}{\epsilon^2(\mathbf{r})}. \tag{42}$$

Such a complex dependence on $\epsilon(\mathbf{r})$ causes further complications when we introduce a small perturbation $\delta\epsilon(\mathbf{r})$, needed for computing sensitivity. Unlike Eq. (1), the linear perturbation term in $\kappa^2(\mathbf{r})$ becomes

$$\delta\kappa^2(\mathbf{r}) \simeq k^2\, \delta\epsilon(\mathbf{r}) - \frac{\nabla^2\epsilon(\mathbf{r})}{2\,\epsilon^2(\mathbf{r})}\, \delta\epsilon(\mathbf{r}) + \tfrac{3}{2}\frac{\nabla\epsilon(\mathbf{r}) \cdot \nabla\epsilon(\mathbf{r})}{\epsilon^3(\mathbf{r})}\, \delta\epsilon(\mathbf{r}) - \tfrac{3}{2}\frac{\nabla\epsilon(\mathbf{r}) \cdot \nabla\delta\epsilon(\mathbf{r})}{\epsilon^2(\mathbf{r})}. \tag{43}$$

Next, we apply the same theoretical approach as in Sec. II A to derive the appropriate expression for the TE sensitivity (see Appendix A). We arrive at

$$S(\mathbf{r}_0) = -\delta V \left(k^2 - \frac{\nabla^2\epsilon(\mathbf{r}_0)}{2\,\epsilon^2(\mathbf{r}_0)} + \frac{3}{2}\frac{\nabla\epsilon(\mathbf{r}_0) \cdot \nabla\epsilon(\mathbf{r}_0)}{\epsilon^3(\mathbf{r}_0)} - \frac{3}{2}\nabla\left(\frac{\nabla\epsilon(\mathbf{r}_0)}{\epsilon^2(\mathbf{r}_0)}\right)\right) \mathrm{Re}[\phi_h(\mathbf{r}_0) h_0(\mathbf{r}_0)], \tag{44}$$

where $\phi_h(\mathbf{r}_0)$ and $h_0(\mathbf{r}_0)$ are defined analogously to $\phi(\mathbf{r}_0)$ and $E_0(\mathbf{r}_0)$ in Eq. (8). As in Eq. (8), this expression is exact in the limit of small perturbation. In contrast to the scalar case, Eq. (44) depends on derivatives of the dielectric function, making it cumbersome for numerical modeling.

Here, we present arguments that the additional terms in the parentheses in Eq. (44) can, in fact, be insignificant in many systems. Specifically, we consider two examples of such disordered media:

Case I: a biological medium such as weakly scattering tissue. The dielectric function in this case varies rather weakly—the characteristic fluctuation $\overline{\delta\epsilon(\mathbf{r}_0)^2}^{1/2}$ is much smaller than the mean value $\overline{\epsilon(\mathbf{r}_0)}$. Furthermore, the characteristic spatial extent of these variations L_ϵ is much

larger than the wavelength of light. These two facts allow us to obtain a rough estimate for the gradient terms in Eq. (44) as $\left(\overline{\delta\epsilon(\mathbf{r}_0)^2}/\overline{\epsilon(\mathbf{r}_0)}^2\right)/L_\epsilon^2$ and to conclude that they should be negligible compared to the first term k^2.

Case II: the planar scattering media considered in Ref. [32]. This is also used as a model in our scalar simulations in Sec. III. Here, we consider a uniform (but large $\epsilon \sim 2.85^2$) dielectric function with a small concentration of air holes ($\epsilon_{\text{air}} = 1$). In such a medium, the variations of $\epsilon(\mathbf{r}_0)$ are limited to the interfaces between the dielectric and air holes, making them statistically rare. Therefore, although the nonzero contributions are of the order of unity, their statistical contribution (volume average) is small. Specifically, in our numerical model, we estimate that this contribution is of the order of $(\Delta x/r) \times f \ll 1$. Here, Δx is the pixel size, r is the radius of the hole, and f is the filling fraction of the air holes. This estimate shows that this contribution, limited to only interfaces between the dielectric and air, vanishes as $\Delta x/r \to 0$. Consequently, in this case too, we are justified in omitting the gradient terms, and we obtain the following simplified expression for the TE optical sensitivity:

$$\mathcal{S}(\mathbf{r}_0) \simeq -k^2 \delta V \mathrm{Re}[\phi_h(\mathbf{r}_0) h_0(\mathbf{r}_0)]. \tag{45}$$

This is the expression we are going to investigate numerically in the next section.

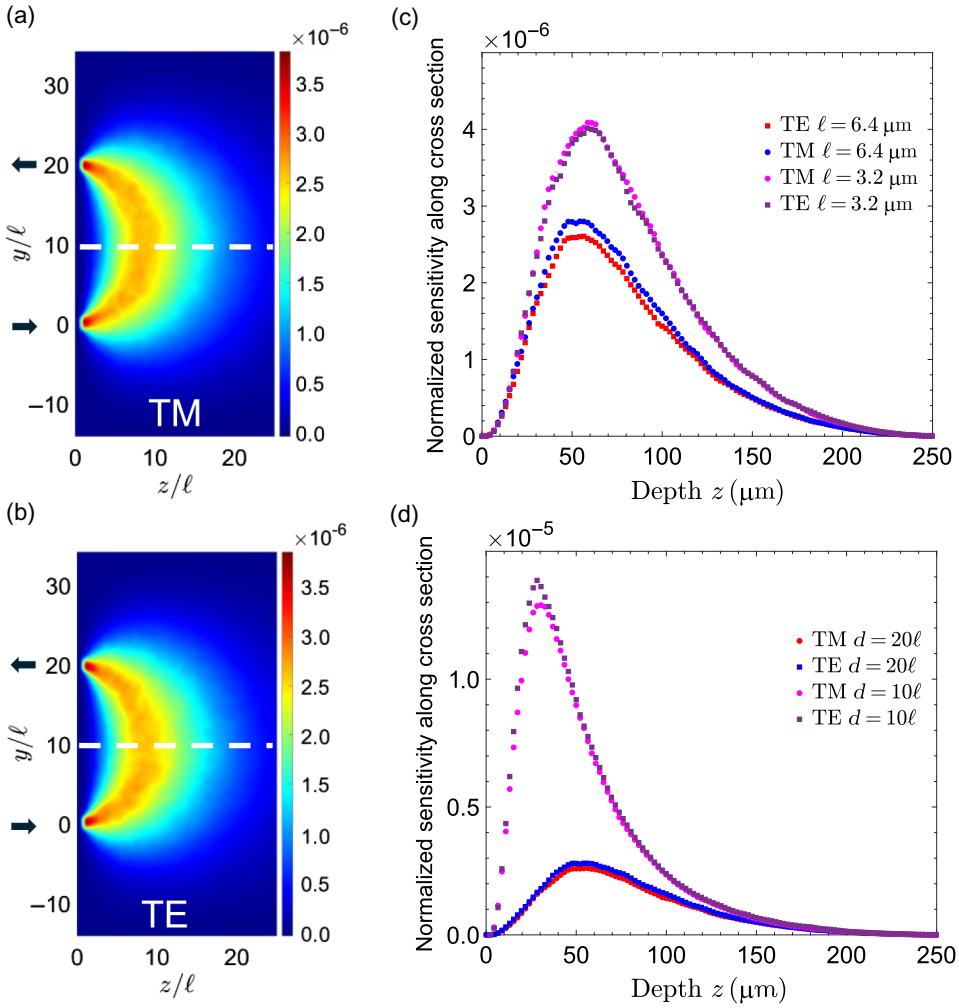

FIG. 7. Effect of polarization on microscopic optical sensitivity. (a),(b) Sensitivity maps computed using Eqs. (8) for TM polarization and (45) for TE polarization, respectively. Results are averaged over 1000 disorder realizations. The microscopic disorder in (b) is adjusted to yield the same transport mean free path as in (a), $\ell = 6.4$ μm. The sensitivity distributions show strong agreement in both shape and magnitude. (c) Depth cross section along the midplane [dashed lines in panels (a) and (b)], comparing the TE and TM polarizations for different values of ℓ. The input-output separation is $d = 20\ell$. (d) Further comparison of the TE and TM sensitivity at fixed $\ell = 6.4$ μm, showing that the agreement persists across different geometrical parameters, such as the input-output port separation d.

TABLE I. Sensitivity $\mathcal{S}(r_0)$ evaluated along the banana trajectory for three excitation schemes: random input, PC input, and MRE excitation.

	Random input sensitivity	PC enhancement η^{PC}	MRE enhancement η^{MRE}
2D:	$-\delta V \times \frac{1}{\pi^2} \times \frac{N_1 N_2}{d^2}$	$\times N_1$	$\times \left(1+\sqrt{\frac{N_1}{N_2}+N_1 C_2}\right)^2$
3D:	$-\delta V \times \frac{9}{8\pi k} \times \frac{N_1 N_2}{d^4 \cos\theta}$	$\times N_1$	$\times \left(1+\sqrt{\frac{N_1}{N_2}+N_1 C_2}\right)^2$

B. Numerical analysis

We use the numerical model described in detail in Sec. III A, with the only difference being that we now consider the TE polarization using the MESTI software package [62]. The shaped wavefront used to excite the maximum remission eigenchannel is constructed from the remission matrix $\mathcal{R}$, which, in this case, represents the field remission matrix for the out-of-plane component of the magnetic field. Our goal is to compare the vector-wave (TE—two components of the electric field) sensitivity to the scalar (TM—one component of the electric field) case considered in Sec. III A. Figures 7(a) and 7(b) show 2D sensitivity maps $\mathcal{S}(\mathbf{r}_0)$ in the TM and TE polarization, respectively. The data are statistically averaged over 1000 realizations. The input and output widths $W_1 = W_2$ are 10 μm and the input-output separation is $d = 20 \times \ell$. We set the microscopic disorder parameters, specifically the air-hole size and density, for the TE case such that the macroscopic scattering parameter—the transport mean free path—matches that in the scalar simulation, $\ell = 6.4$ μm. We observe the typical banana profile in both cases, as the sensitivity maps agree quantitatively. This can also be observed from the cross section of each map along the midplane [dashed lines in Figs. 7(a) and 7(b)] shown in Fig. 7(c). To confirm that the agreement between the scalar and vector cases is not accidental, we varied the microscopic disorder in both cases to reduce the mean free path to $\ell = 3.2$ μm. Again, we observe good agreement between the simulations [see Fig. 7(c)]. We also verified that geometrical parameters, such as the separation distance d between the input and output ports, do not introduce any discrepancy between the scalar and vector results. Figure 7(d) shows that the agreement is indeed preserved irrespective of the value of d.

To provide insight into the polarization invariance of remission sensitivity, we make two complementary observations—one formal and one physical. Formally, Eq. (45), derived for TE-polarized vector waves in 2D, has the same mathematical structure as Eq. (8) for scalar (TM) waves. As discussed in Sec. IV A, such structural similarity is expected for a broad class of scattering systems. This supports the conclusion that the optical sensitivity, defined via these equations, should be largely polarization independent. Physically, it is difficult to identify any mechanism by which a particular component of the electric field would be systematically favored *inside* the diffusive scattering system once the scattering direction becomes completely randomized.

V. CONCLUSION

In this work, we developed a microscopic theory for optical sensitivity that remains valid under coherent wavefront control and verified its consistency with diffusion-based models in the appropriate limit. This formalism revealed how sensitivity can be systematically enhanced via phase conjugation and remission eigenchannels, and it enabled quantitative predictions of the enhancement achieved with these input excitations. Although the numerical simulations presented here were conducted in 2D, the theoretical description remains applicable to 3D systems.

To summarize our results, we evaluated the sensitivity map along the "banana" trajectory—a half-circle path of radius $d/2$ connecting input and output (see Table I). This shape corresponds to the spatial profile of sensitivity under random input. While this profile is preserved under the MRE and PC excitations, the required input wavefronts differ: the MRE uses a fixed input wavefront found by maximizing remission, whereas PC requires distinct inputs for each target position. In the 2D case, sensitivity is nearly constant along the path, with PC input yielding a factor of N_1 enhancement η^{PC} due to constructive interference of time-reversed paths. The MRE yields a sensitivity enhancement η^{MRE}, which can be predicted either by the FRM theory or by the effective Marchenko-Pastur model reported in Table I, both incorporating the effect of long-range correlation C_2 (see Appendices G and H). In 3D, the sensitivity varies along the banana geometry as a function of polar angle θ (see Appendix D); however, both the PC and MRE enhancement factors remain the same as in 2D. That said, the contribution of C_2 to η^{MRE} is expected to be much smaller, if not insignificant, in most 3D systems where $\ell \gg \lambda$. This implies that, in 3D, the dominant mechanism for remission or sensitivity enhancement stems from constructive interference, which is preserved due to the deterministic nature of coherent wave transport.

We note two important considerations that motivate the practical implementation of coherent wavefront control strategies. First, the decay of sensitivity with source-detector separation is more severe in three dimensions: while in 2D the sensitivity scales as $\mathcal{S}^{2D} \propto 1/d^2$, in 3D it follows $\mathcal{S}^{3D} \propto 1/d^4$, making the signal diminish even more rapidly with depth (c.f. Table I and Appendix D). Second, the numerical studies in Secs. III and IV focused on a localized absorber used to define sensitivity but did not account for attenuation due to absorption throughout the bulk medium, which is common in biological tissue samples. While the microscopic expression for sensitivity remains unchanged in the presence of absorption, the resulting spatial profile of the sensitivity map does change. As we demonstrated in our earlier work [32], bulk absorption makes the banana-shaped sensitivity map shallower. The above considerations motivate further study and demonstrate the potential of WFS to enhance signal strength through constructive interference, counteracting the degradation of sensitivity caused by both geometric spreading and attenuation.

From a practical standpoint, MREs offer a unique opportunity—they *maximize* the detection sensitivity throughout the entire imaging volume, while only requiring knowledge of the remission matrix, which can be obtained *noninvasively*. Furthermore, our analysis of sensitivity fluctuations in Appendix F shows that, in addition to enhancing the mean sensitivity, MREs also exhibit reduced realization-to-realization variability compared to random input. This robustness ensures that standard inverse-problem techniques can still be applied with a wavefront-shaped input, now with a significantly improved signal-to-noise ratio and consequently greater penetration depth.

The next challenge is to translate these insights into experimental implementations that can overcome the constraints of conventional DOT. The use of dynamic wavefront control in remission-based imaging needs to be explored in live biological systems, where temporal variations in tissue properties introduce additional complexity. Moreover, the question remains whether the principles demonstrated here can be extended to fluorescence and other optical contrast mechanisms that operate under highly scattering conditions.

Beyond imaging, these results point to a broader class of problems in wave physics where coherent control can be used to selectively enhance signal extraction in complex media. The ability to enhance and/or reshape sensitivity maps in a deterministic way suggests applications in adaptive sensing, optogenetics, and noninvasive diagnostics, where penetration depth and resolution are fundamentally limited by scattering. The real impact of this approach will come from experimental validation and the integration of computational wavefront control into next-generation imaging systems.

ACKNOWLEDGMENTS

This work is supported partly by the U.S. National Science Foundation (NSF) under Grants No. DMR-1905442 and No. DMR-1905465, by the U.S. Office of Naval Research (ONR) under Grant No. N00014-221-1-2026, and by the French Government under the program Investissements d'Avenir. Extensive numerical simulations in this work were carried out on the Mill high-performance computing (HPC) cluster [73] at Missouri University of Science and Technology. P.J. and A.Y. gratefully acknowledge Predrag Lazic for technical assistance and IT support.

DATA AVAILABILITY

The data that support the findings of this article are not publicly available. The data are available from the authors upon reasonable request.

APPENDIX A: PERTURBATIVE APPROACH TO DIFFUSE INTENSITY

The intensities $\bar{I}_0(\mathbf{r})$ and $\bar{I}(\mathbf{r})$, before and after a perturbation is introduced, satisfy the diffusion equation

$$-D\nabla^2 \bar{I}_0(\mathbf{r}) = 0, \tag{A1}$$

$$\left[-D\nabla^2 + v_E \delta\mu(\mathbf{r})\right] \bar{I}(\mathbf{r}) = 0. \tag{A2}$$

Here, v_E is the energy velocity (equal to the phase velocity c/n in the absence of resonant scattering), D is the diffusion coefficient, and $\delta\mu(\mathbf{r})$ is a local perturbation in absorption. Although we assumed above that the diffusion coefficient is spatially invariant and absorption is zero in the absence of the perturbation, this description can be straightforwardly generalized to include these effects. Inclusion of such effects would simply detract from our main goal of comparing and contrasting the diffusive picture below with the microscopic treatment in Sec. II A.

The leading correction to $\bar{I}_0(\mathbf{r})$ can be estimated perturbatively as

$$\bar{I}(\mathbf{r}) \simeq \bar{I}_0(\mathbf{r}) + \int d\mathbf{r}' d\mathbf{r}'' \, G_0^{\mathrm{I}}(\mathbf{r}, \mathbf{r}') \, \mathcal{V}^{\mathrm{I}}(\mathbf{r}', \mathbf{r}'') \, \bar{I}_0(\mathbf{r}''), \tag{A3}$$

where $G_0^{\mathrm{I}}(\mathbf{r}, \mathbf{r}')$ is the Green's function of the diffusion equation

$$-D\nabla^2 G_0^{\mathrm{I}}(\mathbf{r}, \mathbf{r}') = \delta(\mathbf{r} - \mathbf{r}'), \tag{A4}$$

and the perturbation, which is assumed to have a linear size much smaller than the transport mean free path ℓ, is

represented by the delta potential

$$\mathcal{V}^{\mathrm{I}}(\mathbf{r}) = \tilde{\mathcal{V}}^{\mathrm{I}}\,\delta(\mathbf{r}-\mathbf{r}_0), \quad \text{with} \quad \tilde{\mathcal{V}}^{\mathrm{I}} = -v_E\,\delta\mu\,\delta V. \tag{A5}$$

Substituting Eq. (A5) into Eq. (A3) gives the perturbation of intensity $\overline{\delta I}(\mathbf{r}) = \overline{I}(\mathbf{r}) - \overline{I}_0(\mathbf{r})$ similar to Eq. (3),

$$\overline{\delta I}(\mathbf{r}) = \tilde{\mathcal{V}}^{\mathrm{I}}\,G_0^{\mathrm{I}}(\mathbf{r},\mathbf{r}_0)\,\overline{I}_0(\mathbf{r}_0). \tag{A6}$$

Comparing this to Eq. (3), we find $\delta\mu = k\epsilon''$.

Equation (A6) is used in Sec. II C to evaluate the change in the flux at the detector in response to the perturbation.

APPENDIX B: PROOF OF THE GREEN'S FUNCTION IDENTITY EQ. (31) WITHIN THE DIFFUSIVE APPROXIMATION

To evaluate the left-hand side in Eq. (31), we expand each Green's function over all possible scattering paths, selecting only those paths that do not accumulate phase terms dependent on the specific disorder configuration. These paths are represented by the ladder diagram shown in Fig. 8. We find

$$\overline{\langle\chi_b|G_0|\mathbf{r}_0\rangle\langle\mathbf{r}_0|G_0|\chi_a\rangle\langle\chi_b|G_0|\chi_a\rangle^*} = \int d\mathbf{r}_1 d\mathbf{r}_1' d\mathbf{r}_2 d\mathbf{r}_2' \left|\langle\chi_b|\bar{G}_0|\mathbf{r}_2'\rangle\right|^2 \Gamma(\mathbf{r}_2',\mathbf{r}_2)\langle\mathbf{r}_2\mathbf{r}_2|\hat{W}(\mathbf{r}_0)|\mathbf{r}_1\mathbf{r}_1\rangle\,\Gamma(\mathbf{r}_1,\mathbf{r}_1')\left|\langle\mathbf{r}_1'|\bar{G}_0|\chi_a\rangle\right|^2, \tag{B1}$$

which involves the 4-rank tensor $\hat{W}(\mathbf{r}_0) = \left[\bar{G}_0\,|\mathbf{r}_0\rangle\,\langle\mathbf{r}_0|\,\bar{G}_0\right] \otimes \bar{G}_0^\dagger$. The kernel $W(\mathbf{r}_0,\mathbf{r}_2,\mathbf{r}_1) \equiv \langle\mathbf{r}_2\mathbf{r}_2|\,\hat{W}(\mathbf{r}_0)\,|\mathbf{r}_1\mathbf{r}_1\rangle$ can be expressed as

$$W(\mathbf{r}_0,\mathbf{r}_2,\mathbf{r}_1) = \langle\mathbf{r}_2|\bar{G}_0|\mathbf{r}_0\rangle\langle\mathbf{r}_0|\bar{G}_1|\mathbf{r}_1\rangle\langle\mathbf{r}_2|\bar{G}_0|\mathbf{r}_1\rangle^*, \tag{B2}$$

as illustrated in Fig. 8. This gives a non-negligible contribution to the integral Eq. (B1) for $\mathbf{r}_1$ and $\mathbf{r}_2$ in the vicinity of $\mathbf{r}_0$. Using $\Gamma(\mathbf{r}_1,\mathbf{r}_1') \simeq \Gamma(\mathbf{r}_0,\mathbf{r}_1')$ and $\Gamma(\mathbf{r}_2',\mathbf{r}_2) \simeq \Gamma(\mathbf{r}_2',\mathbf{r}_0)$, we get

$$\overline{\langle\chi_b|G_0|\mathbf{r}_0\rangle\langle\mathbf{r}_0|G_0|\chi_a\rangle\langle\chi_b|G_0|\chi_a\rangle^*} = K_{b\mathbf{r}_0}W(\mathbf{r}_0)\,K_{\mathbf{r}_0 a}, \tag{B3}$$

where $K_{\mathbf{r}_0 a} = K_{a\mathbf{r}_0}$ is defined as

$$K_{\mathbf{r}_0 a} = \int d\mathbf{r}_1 \Gamma(\mathbf{r}_0,\mathbf{r}_1)\left|\langle\mathbf{r}_1|\bar{G}_0|\chi_a\rangle\right|^2, \tag{B4}$$

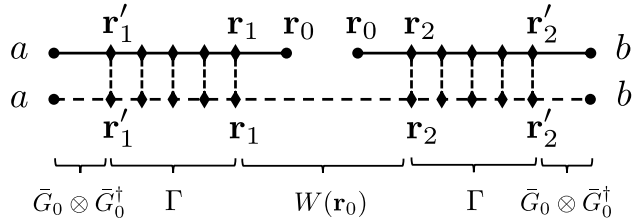

FIG. 8. Leading diagram in the expansion of $\overline{\langle\chi_b|G_0|\mathbf{r}_0\rangle\langle\mathbf{r}_0|G_0|\chi_a\rangle\langle\chi_b|G_0|\chi_a\rangle^*}$. Solid and dashed horizontal lines represent the Green's operators $\bar{G}_0$ and $\bar{G}_0^\dagger$, respectively, while diamonds represent scatterers. Vertical dashed lines connect identical scatterers.

and $W(\mathbf{r}_0) = \int d\mathbf{r}_1 d\mathbf{r}_2 W(\mathbf{r}_0,\mathbf{r}_2,\mathbf{r}_1)$. The integrated kernel is independent of the position $\mathbf{r}_0$ of the perturbation, since

$$W(\mathbf{r}_0) = \langle\mathbf{r}_0|\,\bar{G}_0\bar{G}_0^\dagger\bar{G}_0\,|\mathbf{r}_0\rangle = \int \frac{d\mathbf{q}}{(2\pi)^d}\bar{G}_0(q)^2\bar{G}_0(q)^*. \tag{B5}$$

Using $\bar{G}_0(q) = (k^2 - q^2 - ik/\ell)^{-1}$, explicit calculation in the limit $k\ell \gg 1$ gives

$$W(\mathbf{r}_0) \simeq \frac{i}{8}\frac{\ell^2}{k^2}\left(\frac{k}{\pi}\right)^{\mathcal{D}-2}. \tag{B6}$$

We conclude that the left-hand side of Eq. (31) can be expressed as

$$\overline{\langle\chi_b|G_0|\mathbf{r}_0\rangle\langle\mathbf{r}_0|G_0|\chi_a\rangle\langle\chi_b|G_0|\chi_a\rangle^*} = \frac{i}{8}\frac{\ell^2}{k^2}\left(\frac{k}{\pi}\right)^{\mathcal{D}-2}K_{b\mathbf{r}_0}\,K_{\mathbf{r}_0 a}. \tag{B7}$$

The right-hand side of Eq. (31) can also be expressed in terms of the product $K_{b\mathbf{r}_0}K_{\mathbf{r}_0 a}$. Indeed, in the diffusive limit, we have

$$\begin{aligned}
&\overline{|\langle\mathbf{r}_0|G_0|\chi_a\rangle|^2} \\
&= \int d\mathbf{r}_1 d\mathbf{r}_2 \left|\langle\mathbf{r}_0|\bar{G}_0|\mathbf{r}_2\rangle\right|^2 \Gamma(\mathbf{r}_2,\mathbf{r}_1)\left|\langle\mathbf{r}_1|\bar{G}_0|\chi_a\rangle\right|^2 \\
&\simeq \left[\int d\mathbf{r}_2 \left|\langle\mathbf{r}_0|\bar{G}_0|\mathbf{r}_2\rangle\right|^2\right]\int d\mathbf{r}_1\Gamma(\mathbf{r}_0,\mathbf{r}_1)\left|\langle\mathbf{r}_1|\bar{G}_0|\chi_a\rangle\right|^2 \\
&= \frac{\ell}{4k}\left(\frac{k}{\pi}\right)^{\mathcal{D}-2}K_{\mathbf{r}_0 a}.
\end{aligned} \tag{B8}$$

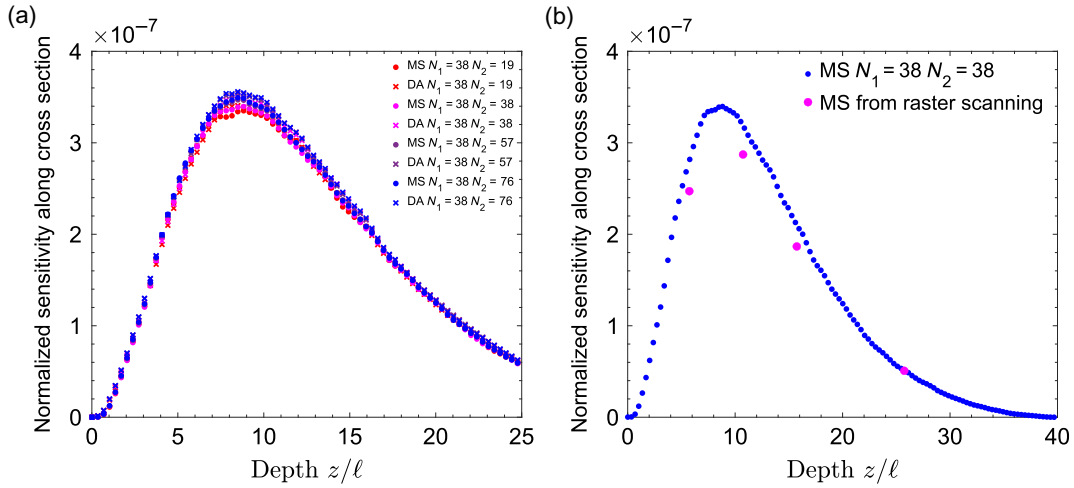

FIG. 9. Comparison between the MS and DA results under random input excitation for asymmetric input and output port widths ($W_1 \neq W_2$). (a) Simulated sensitivity maps for systems with transport mean free path $\ell = 6.4$ μm, using different input and output width combinations (in μm): 10×5, 10×10, 10×15, and 10×20. Excellent agreement is observed in all cases. (b) Validation of the microscopic sensitivity formula: results obtained using the second expression in Eq. (8) (blue circles) are compared with direct brute-force calculations based on the first part of Eq. (8) (red circles), confirming consistency.

This result implies that Eq. (B7) can be written as

$$\overline{\langle\chi_b|G_0|\mathbf{r}_0\rangle\langle\mathbf{r}_0|G_0|\chi_a\rangle\langle\chi_b|G_0|\chi_a\rangle^*} = 2i\left(\frac{\pi}{k}\right)^{\mathcal{D}-2}\overline{|\langle\chi_b|G_0|\mathbf{r}_0\rangle|^2}\;\overline{|\langle\mathbf{r}_0|G_0|\chi_a\rangle|^2}, \quad \text{(B9)}$$

and the identity Eq. (31) then follows naturally.

APPENDIX C: ASYMMETRIC CASES FOR RANDOM AND COHERENT INPUT SENSITIVITIES

In Sec. III B, Fig. 4, we showed the computation of the normalized sensitivity for the random input excitation for the symmetric configuration with $W_1 = W_2$. In Fig. 9(a), we also include the numerical results for asymmetric input and output cases and observe perfect agreement irrespective of the ratio between W_1 and W_2. This provides further support for our normalization procedure in Sec. II E.

Furthermore, in Fig. 9(b), we have applied the first part of Eq. (8). This is the serial way to compute optical sensitivity by taking the ratio between the change of the output flux and the strength of the perturbation [see Fig. 3(a)]. Numerically, we added a small amount of absorption in a square area of $\ell \times \ell$, placed at several z values along the center line. Good agreement with the sensitivity map calculation confirms the validity of the microscopic approach in Sec. II A.

APPENDIX D: DIFFUSION APPROXIMATION FOR SENSITIVITY IN THE REMISSION GEOMETRY: ANALYTICAL RESULT

In the remission geometry considered in Sec. III, a closed-form expression for optical sensitivity, Eq. (28), can be obtained in 2D and 3D. To this end, we begin with the normalized sensitivity, Eq. (32), in terms of the random input intensities

$$\bar{\mathfrak{s}}_{\rm diff}(\mathbf{r}_0) = -\frac{1}{N_1 N_2}\left(\frac{\pi}{k^2}\right)^{\mathcal{D}-2}\bar{I}^{\rm RI}_{\rm in}(\mathbf{r}_0)\,\bar{I}^{\rm RI}_{\rm out}(\mathbf{r}_0). \quad \text{(D1)}$$

Here, the input and output intensities can be found by solving the 2D or 3D diffusion equation in semi-infinite geometry $z > 0$. At $z = 0$, we apply open boundary conditions with an extrapolation length z_e [49]. We also assume that the widths of the input and output, located at $y = 0, d$ [see for example Fig. 4(a)] are much smaller than their separation $W_1, W_2 \ll d$. The normalization adopted in Sec. II C assumes that N_1 units of dimensionless flux are used to excite the system. The source of diffusive waves is $\nabla \cdot \mathbf{J}_{\rm ball}$, where $\mathbf{J}_{\rm ball} = c/(2n_{\rm eff}k) \times e^{-z/\ell}\delta(y)$ is the ballistic (unscattered) flux. The normalization factor $[c/2kn_{\rm eff}]$ is obtained from the microscopic wave equation [62].

In 2D, we find

$$\bar{I}^{\rm RI,2D}_{\rm in}(\mathbf{r}_0) = \frac{c}{2kn_{\rm eff}}\frac{N_1}{\pi D}\frac{\ell\, z_0}{(z_0+z_e)^2+y_0^2}. \quad \text{(D2)}$$

Substituting Eq. (D2) into Eq. (D1), we obtain the final result for the normalized sensitivity map,

$$\bar{\jmath}^{\mathrm{2D}}_{\mathrm{diff}}(y_0, z_0) = -\frac{1}{\pi^2 k^2} \frac{z_0^2}{\left[(z_0+z_e)^2 + y_0^2\right]\left[(z_0+z_e)^2 + (y_0-d)^2\right]}. \tag{D3}$$

This is the desired analytical expression used to study the dependence on detector separation in Fig. 4 from Sec. III D. Interestingly, we find that Eq. (D3) is essentially independent of the transport mean free path. Indeed, at distances exceeding the extrapolation length $z_e \sim \ell$, the dependence on ℓ becomes insignificant. In fact, along the crescent banana trajectory, the sensitivity remains nearly constant:

$$\bar{\jmath}^{\mathrm{2D}}_{\mathrm{diff}} \simeq -\frac{1}{\pi^2} \times \frac{1}{k^2 d^2}. \tag{D4}$$

It depends only on the vacuum wave number $k = 2\pi/\lambda_0$ and source-detector separation d. For $\lambda_0 = 1.55$ μm and $d = 128$ μm, we get $\bar{\jmath}_{\mathrm{diff}}(d/2, d/2) \simeq 3.8 \times 10^{-7}$, which agrees with the microscopical numerical calculations reported in Fig. 4.

The 3D result can be obtained analogously by using the appropriate expression for the Green's function. For $\bar{I}^{\mathrm{RI}}_{\mathrm{in}}(\mathbf{r}_0)$, we get

$$\bar{I}^{\mathrm{RI,3D}}_{\mathrm{in}}(\mathbf{r}_0) = \frac{c}{2kn_{\mathrm{eff}}} \frac{N_1}{2\pi D} \frac{\ell\, z_0}{[x_0^2 + y_0^2 + (z_0+z_e)^2]^{3/2}}, \tag{D5}$$

where the normalization factor $c/2kn_{\mathrm{eff}}$ remains the same as in 2D. Subsequently, we get the final dimensionless expression for the 3D sensitivity map as

$$\bar{\jmath}^{\mathrm{3D}}_{\mathrm{diff}}(\mathbf{r}_0) = -\frac{9}{16\pi k^4} \frac{z_0^2}{\left[x_0^2 + y_0^2 + (z_0+z_e)^2\right]^{3/2}\left[x_0^2 + (y_0-d)^2 + (z_0+z_e)^2\right]^{3/2}}. \tag{D6}$$

Similar to Eq. (D3), Eq. (D6) does not significantly depend on the transport mean free path. Parameterizing the position along the banana trajectory of radius $d/2$ with a polar angle θ, we get the simplified expression

$$\bar{\jmath}^{\mathrm{3D}}_{\mathrm{diff}} \simeq -\frac{9}{8\pi} \times \frac{1}{k^4 d^4} \times \frac{1}{\cos\theta}, \tag{D7}$$

which now, in 3D, depends on k, d, and θ. Unlike the 2D expression, Eq. (D4), the sensitivity is no longer constant along the banana. The divergence at $\theta \sim \pm\pi/2$ is prevented by the surface corrections at the level

$$\bar{\jmath}^{\mathrm{3D}}_{\mathrm{diff}} \propto -\frac{1}{k^4 d^3 \ell}. \tag{D8}$$

APPENDIX E: COMPARISON BETWEEN THE RANDOM INPUT AND MAXIMUM REMISSION EIGENCHANNEL PROFILES

Figure 10 highlights a striking and unresolved feature in the behavior of the optical sensitivity under coherent excitation. According to the DA in Sec. II C, the sensitivity map $\bar{\jmath}(\mathbf{r}_0)$ is predicted to be proportional to the product of the input and output intensity profiles at position $\mathbf{r}_0$: $\bar{\jmath}_{\mathrm{DA}}(\mathbf{r}_0) \propto \bar{I}_{\mathrm{in}}(\mathbf{r}_0) \times \bar{I}_{\mathrm{out}}(\mathbf{r}_0)$ [see Eq. (28)]. This is illustrated in Figs. 10(a) and 10(b) for the RI case, where the resulting sensitivity map exhibits the expected banana-shaped profile, consistent with established DOT theory.

When the system is excited with the MRE, a coherent input state with a significantly different internal intensity distribution is produced, as shown in Fig. 10(c). Surprisingly, however, the product $\bar{I}^{\mathrm{MRE}}_{\mathrm{in}}(\mathbf{r}_0) \times \bar{I}^{\mathrm{MRE}}_{\mathrm{out}}(\mathbf{r}_0)$ still results in a map with a similar shape, as shown in Fig. 10(d). This result was discussed in Sec. III C and is referred to as a heuristic DA*. The resemblance of the profiles in Figs. 10(b) and 10(d) is unexpected, but it holds even quantitatively (see Sec. III C). From the analysis in Sec. II C, the DA prediction is not expected to be applicable for coherent input states such as MREs, since the DA assumes statistical independence of input and output fields—a condition clearly violated by the structured nature of MRE excitation. Nonetheless, Fig. 10 suggests that the *spatial structure* of the sensitivity map remains robust, even when the underlying field intensities deviate significantly from those predicted by diffusion.

The origin of this robustness is not presently understood. The fact that the product $\bar{I}^{\mathrm{MRE}}_{\mathrm{in}}(\mathbf{r}_0) \times \bar{I}^{\mathrm{MRE}}_{\mathrm{out}}(\mathbf{r}_0)$ retains a similar shape despite strong modification of each factor individually implies the presence of subtle constraints in the underlying wave transport that are not captured by existing theory. This observation highlights an important open question: why does the DA-inspired structure of the sensitivity map persist even for coherent input states far

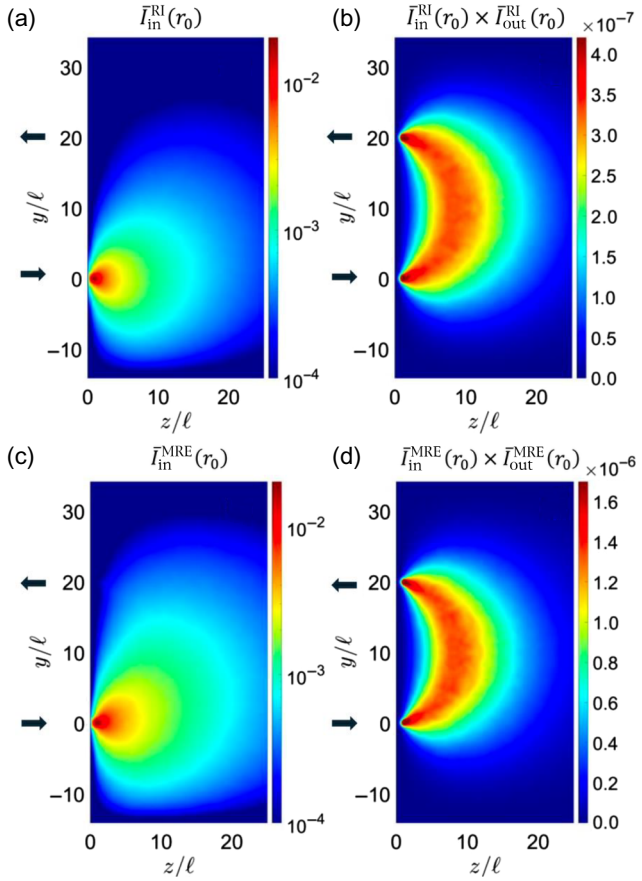

FIG. 10. Comparison between random input and MRE excitation. (a) Simulated input intensity $\bar{I}_{\rm in}^{\rm RI}(\mathbf{r}_0)$ for random input in a system with $\ell = 6.4\ \mu$m, $d = 20\,\ell$ and $W_1 = W_2 = 5\ \mu$m. (b) Product $\bar{I}_{\rm in}^{\rm RI}(\mathbf{r}_0) \times \bar{I}_{\rm out}^{\rm RI}(\mathbf{r}_0)$, representing the normalized sensitivity map for random input, as given by Eq. (28) under the DA. (c) Input intensity $\bar{I}_{\rm in}^{\rm MRE}(\mathbf{r}_0)$ corresponding to the maximal remission eigenchannel. (d) Product $\bar{I}_{\rm in}^{\rm MRE}(\mathbf{r}_0) \times \bar{I}_{\rm out}^{\rm MRE}(\mathbf{r}_0)$, constituting the DA* heuristic for the sensitivity map under MRE excitation, as discussed in Sec. III C.

outside the DA regime? Resolving this will require deeper theoretical insight into why the banana-like profile of sensitivity is preserved even under coherent illumination. One promising direction could be sum rules [69], which are known to produce nontrivial constraints in mesoscopic wave transport.

APPENDIX F: EFFECT OF FLUCTUATIONS ON SENSITIVITY

The results presented in the main text correspond to disorder-averaged quantities. In practice, however, both extrinsic (sample-to-sample) and intrinsic (point-to-point within the same sample) fluctuations play an important role [74] in the interpretation of experimental measurements of sensitivity. Here, we quantify these fluctuations and analyze their relevance for applications such as diffuse optical imaging.

For each disorder realization, we computed the sensitivity averaged over a perturbation area A_P centered in the middle of the banana region. Treating this volume-averaged sensitivity as a single data point, we compiled distributions from 1000 disorder realizations. The results are shown in Fig. 11. Figure 11(a) displays the distribution of ϑ_{A_P} for RI, which is broad with a finite variance. Figure 11(b) shows the distribution for the MRE excitation: the mean sensitivity is increased, while the relative fluctuations are smaller. Thus, MRE achieves both *enhanced mean sensitivity and reduced fluctuations* compared to RI.

Figure 11(c) quantifies the relative fluctuations, $\sigma_{\vartheta_{A_P}}/\bar{\vartheta}_{A_P}$, as a function of perturbation area. Both RI and MRE show a decrease of fluctuations with increasing A_P, but with a weaker scaling than the ideal $1/\sqrt{A_P}$ dependence expected for uncorrelated random contributions. Importantly, across all A_P, the fluctuations of sensitivity under MRE excitation are consistently smaller than those for RI. This robustness resembles the behavior for the intensity of high-transmission eigenchannels in the waveguide geometry, which also exhibits suppressed realization-to-realization fluctuations compared to random inputs [53].

The above results demonstrate that remission eigenchannels are not only advantageous in terms of mean sensitivity but also in terms of statistical stability. Their reduced fluctuations make them particularly promising for diffuse optical imaging applications, where this property should result in an increase in robustness of the inverse-problem algorithms reconstructing the locations of the perturbations from remission measurements.

APPENDIX G: FILTERED RANDOM MATRIX THEORY FOR PREDICTING COHERENT REMISSION ENHANCEMENT

The detailed description of the analytical procedure used for computing remission enhancement by applying filtered random matrix theory can be found in Ref. [32]; however, for the sake of completeness, we will summarize here the overall scheme of the method. In Fig. 6 in Sec. III D, we included solid lines that represent the analytical solutions when computing sensitivity as a function of ℓ and the geometrical parameters d, N_1, and N_2.

As is well known, the scattering matrix fully encodes multiple scattering within the medium; it is a powerful tool that relates arbitrary input fields to their corresponding outputs, and in principle, it allows for the reconstruction or prediction of either (see Fig. 1 in Sec. II A). Thus, to compute the theoretical enhancement, we rely on full knowledge of the scattering matrix. Specifically, access to

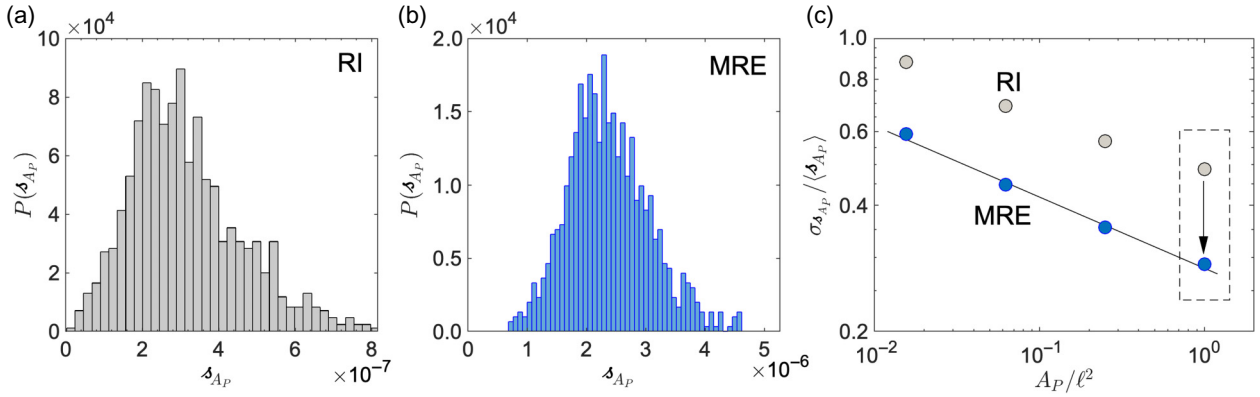

FIG. 11. (a) Distribution of $\mathcal{S}_{A_P}$ sensitivity averaged over a perturbation area $A_P = \ell \times \ell$ under RI excitation. Here, A_P is centered in the middle of the banana region. The histogram is compiled from 1000 disorder realizations. (b) Same as in (a) but for MRE excitation. (c) Log-log plot of relative fluctuations (standard deviation normalized by the mean) computed from $P(\mathcal{S}_{A_P})$ versus perturbation area $A_P = \{1/64, 1/16, 1/4, 1\} \times \ell^2$. Both RI and MRE exhibit similar scaling $\sigma_{\mathcal{S}_{A_P}}/\langle \mathcal{S}_{A_P} \rangle \propto 1/A_P^{\alpha}$ with $\alpha \simeq 0.17$ (solid line). This confirms that fluctuations are suppressed by volume averaging in the $A_P \to \infty$ limit. Importantly, the fluctuations for MRE excitation are significantly suppressed compared to those for random input.

the scattering matrix provides information about the remission matrix $\mathcal{R}$, from which we can compute the eigenvalue probability density function of $\mathcal{R}^\dagger\mathcal{R}$ and its statistical moments. In our setup, light propagates through an open geometry, where input and output channels cover only a small fraction of the total surface area. Therefore, we must also account for incomplete channel control in both injection and detection [32]. The FRM method [64] allows us to model the remission matrix $\mathcal{R}$ as a filtered matrix of dimension $N_2 \times N_1$, drawn from a virtual $M_0 \times M_0$ matrix $\mathcal{R}_0$ characterized by a bimodal distribution of remission eigenvalues with a specific mean value. This model captures the idea that only a fraction of the scattering channels are effectively excited and detected at the injection and remission sites [32]. Both M_0 and the mean $\overline{\rho}_0$ of the bimodal eigenvalue probability density function (PDF) of $\mathcal{R}_0^\dagger\mathcal{R}_0$ are effective parameters of the model, which are unknown *a priori*. A theoretical calculation of the flux and its fluctuations detected in the output port will be used to express M_0 and $\overline{\rho}_0$ in terms of the parameters involved in the remission experiment: the mean free path, the injection remission distance d, and the numbers of input and output spatial channels N_1 and N_2.

According to Refs. [32] and [64], the FRM theory allows one to establish the mathematical relation between the PDFs of $\mathcal{R}^\dagger\mathcal{R}$ and $\mathcal{R}_0^\dagger\mathcal{R}_0$. Below, we give explicit equations for the case $N_1 \geq N_2$, as in Ref. [32]. The case $N_1 \leq N_2$ can be obtained by inverting the roles of N_1 and N_2 in the equations for the eigenvalues ρ. We note, however, that the prediction for the largest eigenvalue $\rho_{\max}$ remains the same in both cases. For $N_1 \geq N_2$, the PDF of the nonzero eigenvalues of $\mathcal{R}^\dagger\mathcal{R}$ is identical to the PDF $P(\rho)$ of the eigenvalues of $\mathcal{R}\mathcal{R}^\dagger$; it is given by $P(\rho) = -\lim_{\eta\to 0^+} \mathrm{Im}[g(\rho + i\eta)]/\pi$, where $g(w)$ is the solution to the following implicit equation [64]:

$$\frac{wm_2 g(w) + 1 - m_2}{m_2 g(w)[wm_2 g(w) + m_1 - m_2]} g\left(\frac{[wm_2 g(w) + 1 - m_2]^2}{m_2 g(w)[wm_2 g(w) + m_1 - m_2]}\right) = 1, \tag{G1}$$

where $m_1 = N_1/M_0$, $m_2 = N_2/M_0$, and

$$g(w) = \frac{1}{w} - \frac{\overline{\rho}_0}{w\sqrt{1-w}} \mathrm{arctanh}\left[\frac{\tanh(1/\overline{\rho}_0)}{\sqrt{(1-w)}}\right]. \tag{G2}$$

Based on Eq. (G1), it is possible to express the moments $P(\rho)$ in terms of the eigenvalue PDF of $\mathcal{R}_0^\dagger\mathcal{R}_0$. Thus, for the first two cumulants, we find [64]

$$\langle \rho \rangle = m_1 \langle \rho_0 \rangle = m_1 \overline{\rho}_0, \tag{G3}$$

$$\mathrm{Var}\left(\frac{\rho}{\langle \rho \rangle}\right) = m_2 \left[\frac{2}{3\overline{\rho}_0} + \frac{1}{m_1} - 2\right]. \tag{G4}$$

We now solve these equations to express the unknown parameters m_1, m_2, and $\overline{\rho}_0$ of Eq. (G1) in terms of the first

two moments, $\langle\rho\rangle$ and $\langle\rho^2\rangle$, to get

$$m_1 = \sqrt{\frac{3\langle\rho\rangle}{2}\left[\beta \mathrm{Var}\left(\frac{\rho}{\langle\rho\rangle}\right) - 1\right] + \left(\frac{3\langle\rho\rangle}{2}\right)^2} + \frac{3\langle\rho\rangle}{2}, \tag{G5}$$

$$m_2 = \frac{m_1}{\beta}, \tag{G6}$$

$$\overline{\rho}_0 = \frac{\langle\rho\rangle}{\rho}, \tag{G7}$$

where $\beta = N_1/N_2$. The above expressions, together with Eq. (G1), allow us to predict the full PDF $P(\rho)$ from the first two moments. The results of this prediction are shown in Ref. [32].

The two first moments can also be evaluated analytically. First, we note that $\langle\rho\rangle = (N_1/N_2)\rho_{\mathrm{RI}}$, where ρ_{RI} is the mean diffusive flux measured in the output port, and it is given by the solution to Fick's law of diffusion,

$$\rho_{\mathrm{RI}} \approx W_2 D \partial_z I(y = d, z = 0), \tag{G8}$$

where $I(y,z)$ is the solution to the stationary diffusion equation,

$$-D\nabla^2 I(y,z) = \delta(y)\delta(z - z_e). \tag{G9}$$

In the previous equations, W_2 is the width of the output, $D = \ell c/2$ is the diffusion coefficient for light, and z_e is the extrapolation length defined in Sec. D. An approximate solution is $I(y,z) \approx z\ell/(\pi D y^2)$ in the limit $y \gg z, \ell$. Using $N_2 = kW_2/\pi$, we get $\rho_{\mathrm{RI}} \approx N_2 k\ell/(kd)^2$ and

$$\langle\rho\rangle \approx N_1 \frac{k\ell}{(kd)^2}. \tag{G10}$$

Next, we need to find the expression for the normalized variance $\mathrm{Var}(\rho/\langle\rho\rangle)$. This variance can be expressed as a function of the full eigenvalues $\tilde{\rho}$ of $\mathcal{R}^\dagger\mathcal{R}$ as

$$\mathrm{Var}\left(\frac{\rho}{\langle\rho\rangle}\right) = \frac{N_2}{N_1}\left[\mathrm{Var}\left(\frac{\tilde{\rho}}{\langle\tilde{\rho}\rangle}\right) + 1\right] - 1, \tag{G11}$$

where we have $\tilde{\rho} = \rho_{\mathrm{RI}}$. To find an expression for $\mathrm{Var}(\tilde{\rho}/\langle\tilde{\rho}\rangle)$, we relate it to the fluctuations in the intensity I_a measured in the output waveguide after exciting the channel a at the input. This is achieved by applying a singular value decomposition to $\mathcal{R}$. By this, we find that $I_a = \sum_n |V_{an}|^2 \tilde{\rho}_n$. As a result, the fluctuations in I_a depend on the fluctuations in $\tilde{\rho}$ and the statistical properties of the matrix V. By assuming that V is randomly distributed in the unitary group [26], we can show that in the limit $M_1 \gg 1$,

$$\mathrm{Var}\left(\frac{\tilde{\rho}}{\langle\tilde{\rho}\rangle}\right) \approx N_1 \mathrm{Var}\left(\frac{I_a}{\langle I_a\rangle}\right). \tag{G12}$$

As explained in Ref. [32], the average in the unitary group makes the result independent of the channel a. It is thus also equal to the fluctuations of intensity $I = |E|^2$ in the output waveguide resulting from a uniform excitation of all modes in the input waveguide. We evaluate the latter by decomposing the field E as a sum of all possible scattering contributions reaching the output waveguide. Using standard diagrammatic techniques, we find

$$\frac{\mathrm{Var} I}{\langle I\rangle^2} = \frac{1}{N_2} + C_2, \tag{G13}$$

where C_2 is the intensity-intensity correlation function, given by

$$C_2 = \frac{1}{4k\ell\langle I(d,0)\rangle^2}\int\int dydz \langle I(y,z)\rangle^2 [\nabla_{y,z} K(d,0;y,z)]^2. \tag{G14}$$

It can be shown that in the limit $d \gg W_1, \ell$, the calculation of C_2 gives

$$C_2 \approx \frac{1}{k\ell}\left[\frac{4}{\pi}\ln\left(\frac{d}{W_1}\right) + \gamma\right], \tag{G15}$$

where numerical simulations produce $\gamma \approx 0.6$. Finally, Eqs. (G11), (G12), and (G13) together give us

$$\mathrm{Var}\left[\frac{\rho}{\langle\rho\rangle}\right] = \frac{N_2}{N_1} + N_2 C_2. \tag{G16}$$

To reach the final step toward the sensitivity-enhancement expression, we need to determine the upper edge $\rho_{\max}$ of the distribution $P(\rho)$. An equation for this quantity can be derived from (G1) (see Eqs. [8] and [9] in the Supporting Information of Ref. [32]). While this equation is exact, it does not provide an explicit analytical expression for $\rho_{\max}$ in terms of N_1, N_2, and C_2; however, an approximate explicit solution can be obtained under the conditions $N_1, N_2 \gg 1$ and $d \gg W_1$, which are satisfied for most of our simulations. The upper edge of $P(\rho)$, as derived in Ref. [26], takes the form

$$\frac{\rho_{\max}}{\langle\rho\rangle} \approx \frac{[(\alpha-1)^{2/3} + (\pi/2)^{2/3}]^2[\alpha - 1 + (\pi/2)^{2/3}(\alpha-1)^{1/3}]}{\alpha(\alpha-1)^{1/3}} + \mathcal{O}(m), \tag{G17}$$

where $\alpha = m/\overline{\rho}_0$. From Eqs. (G5) and (G7), we get

$$\alpha = \frac{m^2}{\langle\rho\rangle} \approx \tfrac{3}{2}\left[\mathrm{Var}\left(\frac{\rho}{\langle\rho\rangle}\right) - 1\right] = \tfrac{3}{2}\left(N_2 C_2 + \frac{N_2}{N_1} - 1\right). \tag{G18}$$

Because of the values of the parameters in our simulations and experiments, we can consider the limit $\alpha \gg 1$ in Eq. (G17),

$$\frac{\rho_{\max}}{\langle\rho\rangle} \approx \alpha + 3\left(\frac{\pi}{2}\right)^{2/3}\alpha^{1/3} - 2 + \mathcal{O}(\alpha^{-1/3}). \tag{G19}$$

This expression allows us to compute the enhancement in the remitted signal, $\rho_{\max}/\rho_{\mathrm{RI}} = (N_1/N_2)\rho_{\max}/\langle\rho\rangle$. We can even make an additional assumption to capture the behavior in the limit $N_2 C_2 \gg 1$ to obtain

$$\frac{\rho_{\max}}{\rho_{\mathrm{RI}}} \approx \frac{3W_1}{2\pi\ell}\left[\frac{4}{\pi}\ln\left(\frac{d}{W_1}\right) + \gamma\right]. \tag{G20}$$

This last expression shows explicitly the strong dependence of the enhancement on the number of input channels and the transport mean free path, as well as a logarithmic dependence on the distance d; however, we remark that the complete dependence on these parameters and the number of output channels is captured by Eq. (G1).

APPENDIX H: EFFECTIVE MARCHENKO-PASTUR MODEL

As explained in Appendix G, while the FRM model is accurate, it does not provide an explicit analytical expression for the remission enhancement for arbitrary aspect ratio N_1/N_2. An alternative model for the remission enhancement is the effective Marchenko-Pastur model, which is less accurate but has the advantages of being simple, intuitive, and providing an explicit expression in terms of N_1, N_2, and C_2. This model was first introduced in Ref. [65] as a simple alternative to the FRM approach in transmission. It was later shown to yield good results for maximizing energy deposition with broadband light [66]. In the present context of remission, this model amounts to assuming that the non-Gaussian remission matrix $\mathcal{R}$ of size $N_2 \times N_1$ can be replaced by an effective Gaussian matrix of size $N_{\mathrm{eff}} \times N_1$, where N_{eff} is the number of effectively independent channels at the output. This number is smaller than N_2 due to long-range correlations at the output, and it is given by $1/N_{\mathrm{eff}} = 1/N_2 + C_2$ [65,66]. In this model, the matrix $\mathcal{R}^\dagger\mathcal{R}$ behaves as a Wishart matrix of aspect ratio N_1/N_{eff}, whose eigenvalue distribution is given by the Marchenko-Pastur law, parameterized solely by N_1/N_{eff}. In particular, in the limit of large matrix size, the upper edge of the distribution, normalized by the mean eigenvalue, yields

$$\frac{\rho_{\max}}{\rho_{\mathrm{RI}}} = \left(1 + \sqrt{\frac{N_1}{N_{\mathrm{eff}}}}\right)^2 = \left(1 + \sqrt{\frac{N_1}{N_2} + N_1 C_2}\right)^2. \tag{H1}$$

To assess the accuracy of the effective Marchenko-Pastur (MP) model in predicting remission enhancement, we consider various combinations of N_1, $1/C_2$, and N_2, looking for systematic deviations between remission/sensitivity enhancements obtained numerically and theoretical predictions. In simulations, we consider the system with the source-detector separation to $d = 20\,\ell$ with $\ell = 6.4$ μm, and we vary the number of degrees of

TABLE II. Comparison of remission enhancement $\eta_{\mathcal{R}}$ obtained from numerical simulations with analytical predictions based on the effective Marchenko-Pastur model and the idealized Marchenko-Pastur model (i.e., $C_2 = 0$), for various input and output port widths. All results correspond to a system with transport mean free path $\ell = 6.4$ μm and source-detector separation $d = 128$ μm.

N_1	N_2	$N1/N2$	C_2	$1/C_2$	$\eta_{\mathcal{R}}$	$\eta_{\mathcal{S}}$	Effective MP	MP
3	57	0.05	0.08	12.7	1.6	1.7	2.4	1.5
3	38	0.08	0.08	12.7	1.7	1.7	2.4	1.6
3	19	0.16	0.08	12.7	1.7	1.8	2.6	2.0
19	38	0.50	0.05	19.4	4.3	4.6	4.9	2.9
38	76	0.50	0.05	21.7	6.1	6.5	6.2	2.9
38	57	0.67	0.05	21.7	6.4	6.9	6.5	3.3
19	19	1.00	0.05	19.4	5.1	5.5	5.8	4.0
38	38	1.00	0.05	21.7	7.0	7.4	7.1	4.0
57	57	1.00	0.05	21.8	8.7	9.4	8.4	4.0
76	76	1.00	0.05	20.8	10.1	11.2	10.0	4.0
57	38	1.50	0.05	21.8	9.6	10.2	9.2	4.9
38	19	2.00	0.05	21.7	8.6	9.3	8.6	5.8
57	19	3.00	0.05	21.8	12.1	12.8	11.3	7.5
19	3	6.33	0.05	19.4	11.3	12.0	13.7	12.4
38	3	12.67	0.05	21.7	21.7	22.0	23.0	20.8
57	3	19.00	0.05	21.8	31.8	32.2	31.9	28.7

freedom at the input and output to scan the relevant interval of the MP parameter C_2 (see Table II). The value of C_2 is computed using Eq. (G15), originally derived in Ref. [32], which provides an analytical expression valid in the limit $d \gg W_1, L$.

As shown, the sensitivity enhancement $\eta_{\mathcal{S}}$ consistently exceeds the remission enhancement $\eta_{\mathcal{R}}$, yet their magnitudes remain close to the effective MP model. This is in agreement with the prediction from Sec. III D that remission enhancement serves as a proxy for global sensitivity enhancement. Moreover, the data corroborate the hypothesis that the MP model with $C_2 = 0$ indeed sets a lower bound on enhancement: any increase beyond this baseline stems from the long-range correlations, whose effect is captured by the C_2 contribution. The observed agreement with theory, despite various finite-size effects, highlights the robustness of the effective MP model in predicting remission enhancement in diffusive media. We also note that the disagreement observed for small N_1 is due to the limitation of the Marchenko-Pastur law, which strictly applies only to matrices of large dimensions.

[1] A. Ishimaru, *Wave Propagation and Scattering in Random Media* (Academic Press, New York, 1978), 1-2.

[2] K. Aki and P. G. Richards, *Quantitative Seismology: Theory and Methods* (W.H. Freeman and Company, San Francisco, 1980).

[3] E. R. Pike and P. C. Sabatier, eds. *Scattering: Scattering and Inverse Scattering in Pure and Applied Science* (Academic Press, San Diego, 2002).

[4] W. C. Chew, *Waves and Fields in Inhomogeneous Media* (IEEE Press, New York, 1995), reprinted by Wiley-IEEE Press, 1999.

[5] J. Bertolotti and O. Katz, Imaging in complex media, Nat. Phys. **18**, 1008 (2022).

[6] L. Wang and H.-i. Wu, *Biomedical Optics: Principles and Imaging* (John Wiley & Sons, Hoboken, NJ, 2007).

[7] B. E. Bouma and G. J. Tearney, *Handbook of Optical Coherence Tomography* (CRC Press, Boca Raton, 2001).

[8] A. Yodh and B. Chance, Spectroscopy and imaging with diffusing light, Phys. Today **48**, 34 (1995).

[9] D. Boas, D. Brooks, E. Miller, C. DiMarzio, M. Kilmer, R. Gaudette, and Q. Zhang, Imaging the body with diffuse optical tomography, IEEE Signal Process. Mag. **18**, 57 (2001).

[10] T. Durduran, R. Choe, W. B. Baker, and A. G. Yodh, Diffuse optics for tissue monitoring and tomography, Rep. Prog. Phys. **73**, 076701 (2010).

[11] F. Scholkmann, S. Kleiser, A. J. Metz, R. Zimmermann, J. Mata Pavia, U. Wolf, and M. Wolf, A review on continuous wave functional near-infrared spectroscopy and imaging instrumentation and methodology, NeuroImage **85**, 6 (2014).

[12] E. E. Vidal-Rosas, A. von Lühmann, P. Pinti, and R. J. Cooper, Wearable, high-density fNIRS and diffuse optical tomography technologies: A perspective, Neurophotonics **10**, 023513 (2023).

[13] F. F. Jöbsis, Noninvasive, infrared monitoring of cerebral and myocardial oxygen sufficiency and circulatory parameters, Science **198**, 1264 (1977).

[14] S. R. Arridge, Optical tomography in medical imaging, Inverse Probl. **15**, R41 (1999).

[15] S. R. Arridge and J. C. Schotland, Optical tomography: Forward and inverse problems, Inverse Probl. **25**, 123010 (2009).

[16] G. Blaney, A. Sassaroli, and S. Fantini, Spatial sensitivity to absorption changes for various near-infrared spectroscopy methods: A compendium review, J. Innov. Opt. Health Sci. **17**, 2430001 (2024).

[17] S.-R. Tsai and M. R. Hamblin, Biological effects and medical applications of infrared radiation, J. Photochem. Photobiol. B: Biol. **170**, 197 (2017).

[18] A. D. Mora, D. Contini, S. Arridge, F. Martelli, A. Tosi, G. Boso, A. Farina, T. Durduran, E. Martinenghi, A. Torricelli, and A. Pifferi, Towards next-generation time-domain diffuse optics for extreme depth penetration and sensitivity, Biomed. Opt. Express **6**, 1749 (2015).

[19] A. Pifferi, D. Contini, A. D. Mora, A. Farina, L. Spinelli, and A. Torricelli, New frontiers in time-domain diffuse optics, a review, J. Biomed. Opt. **21**, 091310 (2016).

[20] A. P. Mosk, A. Lagendijk, G. Lerosey, and M. Fink, Controlling waves in space and time for imaging and focusing in complex media, Nat. Photonics **6**, 283 (2012).

[21] H. Yu, J. Park, K. Lee, J. Yoon, K. Kim, S. Lee, and Y. Park, Recent advances in wavefront shaping techniques for biomedical applications, Curr. Appl. Phys. **15**, 632 (2015).

[22] S. Rotter, and S. Gigan, Light fields in complex media: Mesoscopic scattering meets wave control, Rev. Mod. Phys. **89**, 1 (2017).

[23] S. Gigan *et al.*, Roadmap on wavefront shaping and deep imaging in complex media, J. Phys.: Photonics **4**, 042501 (2022).

[24] H. Cao, A. P. Mosk, and S. Rotter, Shaping the propagation of light in complex media, Nat. Phys. **18**, 994 (2022).

[25] S. Yoon, C. Kim, J. Lee, and W. Choi, Deep optical imaging within complex scattering media, Nat. Rev. Phys. **2**, 141 (2020).

[26] N. Bender, A. Yamilov, A. Goetschy, H. Yilmaz, C. W. Hsu, and H. Cao, Depth-targeted energy deposition deep inside scattering media, Nat. Phys. **18**, 309 (2022).

[27] W. Choi, A. P. Mosk, Q. Han Park, and W. Choi, Transmission eigenchannels in a disordered medium, Phys. Rev. B **83**, 134207 (2011).

[28] M. Davy, Z. Shi, J. Park, C. Tian, and A. Z. Genack, Universal structure of transmission eigenchannels inside opaque media, Nat. Commun. **6**, 6893 (2015).

[29] R. Sarma, A. G. Yamilov, S. Petrenko, Y. Bromberg, and H. Cao, Control of energy density inside a disordered medium by coupling to open or closed channels, Phys. Rev. Lett. **117**, 086803 (2016).

[30] O. S. Ojambati, H. Yılmaz, A. Lagendijk, A. P. Mosk, and W. L. Vos, Coupling of energy into the fundamental

diffusion mode of a complex nanophotonic medium, New J. Phys. **18**, 043032 (2016).
[31] R. Carminati and J. C. Schotland, *Principles of Scattering and Transport of Light* (Cambridge University Press, Cambridge, 2021).
[32] N. Bender, A. Goetschy, C. W. Hsu, H. Yilmaz, P. Jara, A. Yamilov, and H. Cao, Coherent enhancement of optical remission in diffusive media, Proc. Natl. Acad. Sci. **119**, 1 (2022).
[33] P. Sheng, *Introduction to Wave Scattering, Localization, and Mesoscopic Phenomena*, Springer Series in Materials Science Vol. 88 (Springer, 2006), 2nd ed.
[34] C. W. J. Beenakker, Random-matrix theory of quantum transport, Rev. Mod. Phys. **69**, 731 (1997).
[35] J. C. Schotland, Inverse scattering methods for diffuse optical tomography, Inverse Probl. **13**, R1 (1997).
[36] Z. Yaqoob, D. Psaltis, M. S. Feld, and C. Yang, Optical phase conjugation for turbidity suppression in biological samples, Nat. Photonics **2**, 110 (2008).
[37] M. Fink, D. Cassereau, A. Derode, C. Prada, P. Roux, M. Tanter, J.-L. Thomas, and F. Wu, Time-reversed acoustics, Rep. Prog. Phys. **63**, 1933 (2000).
[38] D. Fisher and P. Lee, Relation between conductivity and transmission matrix, Phys. Rev. B **23**, 6851 (1981).
[39] S. M. Popoff, G. Lerosey, R. Carminati, M. Fink, A. C. Boccara, and S. Gigan, Image transmission through an opaque material, Nat. Commun. **1**, 81 (2010).
[40] A. P. Mosk, A. Lagendijk, G. Lerosey, and M. Fink, Controlling waves in space and time for imaging and focusing in complex media, Nat. Photonics **6**, 283 (2012).
[41] L. V. Wang and J. Zhao, Photoacoustic tomography: Principles and advances, Nat. Photonics **7**, 503 (2013).
[42] M. Fink, Time reversed acoustics, Phys. Today **50**, 34 (1997).
[43] P. Ambichl, A. Brandstötter, J. Böhm, M. Kühmayer, U. Kuhl, and S. Rotter, Focusing inside disordered media with the generalized Wigner–Smith operator, Phys. Rev. Lett. **119**, 033903 (2017).
[44] M. Horodynski, M. Kühmayer, A. Brandstötter, K. Pichler, Y. V. Fyodorov, U. Kuhl, and S. Rotter, Optimal wave fields for micro-manipulation in complex scattering environments, Nat. Photonics **14**, 149 (2020).
[45] P. del Hougne, K. B. Yeo, P. Besnier, and M. Davy, Coherent wave control in complex media with arbitrary wavefronts, Phys. Rev. Lett. **126**, 193903 (2021).
[46] D. Bouchet, S. Rotter, and A. P. Mosk, Maximum information states for coherent scattering measurements, Nat. Phys. **17**, 564 (2021).
[47] J. C. Schotland, J. C. Haselgrove, and J. S. Leigh, Photon hitting density, Appl. Opt. **32**, 448 (1993).
[48] J. C. Schotland and V. A. Markel, Inverse scattering with diffusing waves, J. Opt. Soc. Am. A **18**, 2767 (2001).
[49] E. Akkermans and G. Montambaux, *Mesoscopic Physics of Electrons and Photons* (Cambridge University Press, New York, 2007).
[50] M. C. W. van Rossum and T. M. Nieuwenhuizen, Multiple scattering of classical waves: Microscopy, mesoscopy, and diffusion, Rev. Mod. Phys. **71**, 313 (1999).
[51] W. Cui, C. Kumar, and B. Chance, in *Proceedings of SPIE - Time-Resolved Spectroscopy and Imaging of Tissues*, Vol. 1431 (SPIE, Los Angeles, CA, United States, 1991), p. 180.
[52] S. Fantini, G. Blaney, and A. Sassaroli, Transformational change in the field of diffuse optics: From going bananas to going nuts, J. Innov. Opt. Health. Sci. **13**, 1930013 (2020).
[53] N. Bender, A. Yamilov, H. Yılmaz, and H. Cao, Fluctuations and correlations of transmission eigenchannels in diffusive media, Phys. Rev. Lett. **125**, 165901 (2020).
[54] R. Sarma, A. Yamilov, S. F. Liew, M. Guy, and H. Cao, Control of mesoscopic transport by modifying transmission channels in opaque media, Phys. Rev. B **92**, 214206 (2015).
[55] A. Yamilov, S. Petrenko, R. Sarma, and H. Cao, Shape-dependence of transmission, reflection and absorption eigenvalue densities in disordered waveguides with dissipation, Phys. Rev. B **93**, 100201(R) (2016).
[56] M. Koirala, R. Sarma, H. Cao, and A. Yamilov, Inverse design of perfectly transmitting eigenchannels in scattering media, Phys. Rev. B **96**, 054209 (2017).
[57] A. G. Yamilov, R. Sarma, B. Redding, B. Payne, H. Noh, and H. Cao, Position-dependent diffusion of light in disordered waveguides, Phys. Rev. Lett. **112**, 023904 (2014).
[58] R. Sarma, A. Yamilov, and H. Cao, Enhancing light transmission through a random medium with inhomogeneous scattering and loss, Appl. Phys. Lett. **110**, 021103 (2017).
[59] A. Taflove and S. C. Hagness, *Computational Electrodynamics: The Finite-Difference Time-Domain Method* (Artech House, Norwood, 2005), 3rd ed.
[60] J. R. Summers, *Universal wavefront transmission through disordered media*, Master's thesis, Missouri University of Science and Technology, 2018.
[61] C. W. Groth, M. Wimmer, A. R. Akhmerov, and X. Waintal, Kwant: A software package for quantum transport, New J. Phys. **16**, 063065 (2014).
[62] H. Lin, Z. Wang, and C. W. Hsu, Fast multi-source nanophotonic simulations using augmented partial factorization, Nat. Comput. Sci. **2**, 815 (2022).
[63] P. Jara, H. C. Lin, C. W. Hsu, H. Cao, and A. Yamilov, Simulation of coherent remission in planar disordered medium, 2023 International Applied Computational Electromagnetics Society Symposium (ACES) , 1 (2022).
[64] A. Goetschy and A. D. Stone, Filtering random matrices: The effect of incomplete channel control in multiple scattering, Phys. Rev. Lett. **111**, 063901 (2013).
[65] C. W. Hsu, S. F. Liew, A. Goetschy, H. Cao, and A. D. Stone, Correlation-enhanced control of wave focusing in disordered media, Nat. Phys. **13**, 497 (2017).
[66] R. McIntosh, A. Goetschy, N. Bender, A. Yamilov, C. W. Hsu, H. Yılmaz, and H. Cao, Delivering broadband light deep inside diffusive media, Nat. Photonics **18**, 744 (2024).
[67] A. Yamilov and H. Cao, Effect of amplification on conductance distribution of a disordered waveguide, Phys. Rev. E **74**, 056609 (2006).
[68] S. F. Liew, S. M. Popoff, A. P. Mosk, W. L. Vos, and H. Cao, Transmission channels for light in absorbing random media: From diffusive to ballistic-like transport, Phys. Rev. B **89**, 224202 (2014).
[69] A. Yamilov, N. Bender, and H. Cao, Sum rules for energy deposition eigenchannels in scattering systems, Opt. Lett. **47**, 4889 (2022).
[70] Y. Guan, O. Katz, E. Small, J. Zhou, and Y. Silberberg, Polarization control of multiply scattered light through random media by wavefront shaping, Opt. Lett. **37**, 4663 (2012).

[71] H. B. de Aguiar, S. Gigan, and S. Brasselet, Polarization recovery through scattering media, Sci. Adv. **3**, e1600743 (2017).

[72] H.-C. Lin and C. W. Hsu, Full transmission of vectorial waves through 3D multiple-scattering media, Opt. Lett. **49**, 5035 (2024).

[73] The Mill HPC Cluster, Missouri University of Science and Technology (2024), https://scholarsmine.mst.edu/the-mill/1/.

[74] P. Fang, L. Zhao, and C. Tian, Concentration-of-measure theory for structures and fluctuations of waves, Phys. Rev. Lett. **121**, 140603 (2018).